Supplement of Earth Syst. Dynam., 17, 695–716, 2026
https://doi.org/10.5194/esd-17-695-2026-supplement
© Author(s) 2026. CC BY 4.0 License.



Earth System Dynamics
Open Access
EGU

Supplement of

Atmospheric river trajectories organise along a global transport network

Tobias Braun et al.

Correspondence to: Tobias Braun (tobias.braun@uni-leipzig.de)

The copyright of individual parts of the supplement might differ from the article licence.

The overall structure of the global ARTN stays consistent between the full and the post-1979 ERA5 period, as well as for MERRA2-based network (Fig. S1). A schematic to better illustrate the construction of the atmospheric river transport network (ARTN) is shown in Fig. S2. Figure S3 demonstrates how rectangular and hexagonal gridding can yield substantially different results at high latitudes, with PageRank being inflated for some rectangular grid cells over the Antarctic interior due to enhanced cell proximity.

As an alternative to AR centroids, we studied ARTNs based on AR core coordinates (Fig. S4) and the AR head (Fig. S5/S6). We found that the latter track AR landfall and inland penetration more appropriately. However, AR head trajectories can be geometrically more complex and non-smooth (see Fig. S5). The fact that some of the observed displacements are caused by ARs deforming rather than actually advancing is an important caveat of the introduced method. If we locate ARs by their head coordinate instead of their centroids, all bands of enhanced edge weight shift closer towards coasts and into inland areas (Fig. S14d-f). Separating both AR catalogs lends further credibility to the main AR hubs identified in Fig. 2 of the main manuscript but also shows that the relative importance of individual hub regions may differ between ARDTs.

Altering the spatial resolution across which we track ARs along a hexagonal grid only weakly modifies the global node strength distribution (Fig. S7a/d/g). AR highways (edges with high EBC, (Fig. S7b/e/h) remain largely robust but are more strongly affected than node strengths, partly giving rise to additional meridional highways both at lower and higher resolution (Fig. S7b/h). Lowering (enhancing) spatial resolution preserves physically sound boundaries of the identified AR basins (Fig. S7c/f/i) but alters the characteristic size and shape of many basins. AR basins at lower resolution are large and less elongated, AR basins at higher resolution are fragmented towards the mid-latitudinal boundaries and (sub)tropics and appear more elongated.

The sensitivity to the other key parameter of the ARTN construction, the threshold ϵ, is showcased in Fig. S8. Higher threshold values may fragment the global ARTN into multiple disconnected components. Different network metrics may exhibit distinct degrees of sensitivity for this parameter as well (Fig. S9): both node strength and EBC decline when ϵ is increased (Fig. S9a/f). Yet, EBC shows a more abrupt decline and AR highways vanish more severely (Fig. S9g/h/i/j).

We investigated three different consensus network schemes (Fig. S10): the simple thresholded averaging approach that is used throughout the manuscript (Fig. S10a), a majority vote approach (Fig. S10b) and a rank-based approach (Fig. S10c). Majority votes compute the median edge weight from edges that are present in at least 75% of the considered AR catalogs. Rank-based votes are derived by replacing edge weights by their percentile rank [0, 1] across all edges in that network. An edge survives if its mean rank (over all networks that cover this area) exceeds ϵ. Large-scale network topology is robustly maintained regardless of the consensus formation scheme.

The four different random network types that were designed as null models for this study appear visually random, apart from the properties conserved from the real ARTN. Four distinct realizations for each model are shown in (Fig. S11). The Fully Random Walker (FRW) model produces spatially isotropic edge weights (Fig. S11a). The Rewired Graph (RWG) model recovers large-scale connectivity but randomizes edges at sub-synoptic scales (Fig. S11b). The Genesis-Constrained Random Walker and the Termination-Constrained Random Walker models reproduce the prominent genesis and termination regions and edge weights fade out from there, respectively (Fig. S11c/d).

Differences between simple AR histograms, node strengths and PageRank values for both catalogs are displayed in Fig. S12 and highlight different notions of node importance.

The ARTN framework also allows to examine vapor transport patterns along edges and nodes. The discretized IVT classifiers used for Fig. 4 (and also Fig. 3a) are defined through the quantiles displayed in Fig S13. The IVT difference log-distributions of both AR catalogs are smoothed using a kernel density estimate for better comparability. While the intervals increase in size towards the distributions' tails, the covered probability mass shrinks. How discretized IVT classes differ for all nodes between DJF/JJA and El Niño/La Niña is shown for both catalogs in Fig. S23.

Comparing the tARget-4 and PIKART-1 ARTNs, we find that the tARget-4 network (Fig. SS14e) suggests considerably higher AR frequencies along edges in polar regions and across some regions of elevated topography, e.g., North America, in line with previous findings that the tARget differs from other ARDTs here Lora et al. (2020). The consensus network synthesizes these discrepancies into a single joint representation. Edge directions are largely consistent between both catalogs (Fig. SS15): mid-latitudinal AR transport orients towards the West with north/southward edges closer to the poles, respectively. Some of the ARs responsible for these north/southward edges make landfall along Arctic/Antarctic coastlines, with potentially destabilizing

impacts Maclennan et al. (2025); Wang et al. (2024). Figure S16 provides a broader overview of catalog uncertainties, including not only PIKART-1 and tARget-4 but also the IPART-1 (extratropics) and AR-CONNECT (mid-latitudes) algorithms.

Clustering coefficients characterize triadic closure, i.e., if a node's neighbour is also its neighbour's neighbour. In the ARTN, this pinpoints regions of cyclical AR transport, e.g. due to orographic barriers (Fig. S17).

Figure S18 shows the overall relationship between the discretized integrated vapor transport (IVT) changes and IVT at landfall displayed spatially in Fig. 3b (separated by AR catalog). The indicated correlation values are used to normalise the defined predictability measure: the maximum predictability is set to the correlation over all spatial locations, averaged over both catalogs. PIKART-1 gives rise to a more well-expressed monotic relationship while the high fraction of low-IVT ARs in tARget-4 yields a more complex relationship. The latter is skewed towards low values which do not appear to have strong predictive power for IVT at landfall.

All edge betweenness centralities (EBC) from the real consensus network are tested against the ones expected from the four null models (Fig. S19). Interestingly, the FRW model yields the largest significance threshold (upper 90%-quantile, Fig. S19a) whereas the more systematic models entail lower EBC. We hypothesize that the reason for this counter-intuitive result could be that in a more random network, edge weights are homogeneously distributed so that many edges can bridge different parts of the network. If thresholded by the highest displayed EBC-threshold from the FRW model (Fig. S19a, orange line), the main AR highways discussed in the manuscript are still deemed significant.

The notion of 'AR highways' prompts the question of how closely individual ARs actually follow them and whether this could offer enhanced predictability. We classify ARs into three groups based on the mean EBC of all edges they traverse: *Conformists* (top 33%-EBC), *Straddlers* (middle 33%-EBC), and *Strays* (bottom 33%-EBC). These categories reflect decreasing alignment with AR highways (Fig. S20a-c). Trajectories were smoothed using B-spline interpolation. While *Conformists* tend to follow AR highways most rigidly, *Straddlers* visibly drift off AR highways more often and behave more intermittently. *Stray* trajectories exhibit marked anomalies, e.g., circular movement, or venture far off the main branches. *Conformists* differ significantly in mean IVT from both *Straddlers* and especially from *Strays* (moderate standardized Wasserstein distance d_w of $0 \leq 0.27 \leq 1$, $p < 0.01$ for two-sided Kolmogorov-Smirnov and Mann-Whitney U-test, Fig. S20d), while the latter two are similar ($d_w = 0.09$). Combined with visible differences in lifetimes (Fig. S20e), this suggests that ARs that stray off highways tend to "live" longer and be more intense.

While Fig. 4 directly shows the AR highways for the seasonally and ENSO-conditioned ARTNs, the underlying networks are shown in Fig. S21. Differences are not as striking as they are through the AR highways but visible. The classification of El Niño/La Niña phases is based on the time series discretization shown in Fig. S22. To better illustrate where seasonal/ENSO-phase induced IVT changes are most pronounced, Fig. 19 plots these differences explicitly. We clearly observe the strongest contrasts in the (sub)tropics whereas in the mid-latitudes, regions of enhanced IVT strengthening/weakening do not shift that strongly. The most marked exceptions are likely the enhanced IVT intensification in boreal summer over the eastern North Atlantic and the eastern North Pacific, as well enhanced IVT depletion towards Australia in austral winter. Figure SS23 shows how IVT differs between the seasonal and ENSO categories.

Evaluation metrics of the non-hierarchical AR basins are shown in Fig. S24. Overall, all continental AR basins are less well-separated and are detected less consistently across distinct runs of Infomap (Fig. S24b/d). Hence, their exact contours cannot be delineated as robustly. Some isolated basins (e.g., over Alaska) exhibit high flow ratios simply due to their low degree of connectivity to other communities (Fig. S24b, purple). Stability and quality of one null model realization per null model are shown in Fig. S25.

In comparison to the four null models, most of the detected AR communities are significantly more stable and well-separated than those obtained from the FRW network model and, on average, also slightly more stable than those detected in the GCW/TCW network models (which naturally have a strong community structure in the genesis/termination regions, respectively) (Fig. S26). Only the RWG network ensemble yields significantly more robust and separated communities, likely since the implemented distance constraint restricts rewiring to local connections, resulting in confined, well-structured communities.

Together with Fig. S27, Table S1 provides an overview of how AR basins are distinguishable in terms of the ARs that they host. While basins are solely defined based on AR transport patterns encapsulated in the global ARTN, we still find substantial differences in the types of ARs that are usually transiting or residing each basin (discussed in the main manuscript).

The identified AR basins are long-term aggregates of the underlying non-stationary transport dynamics. From one season to another, AR basins across many regions differ quite substantially (Fig. S28, further discussed in the main manuscript).

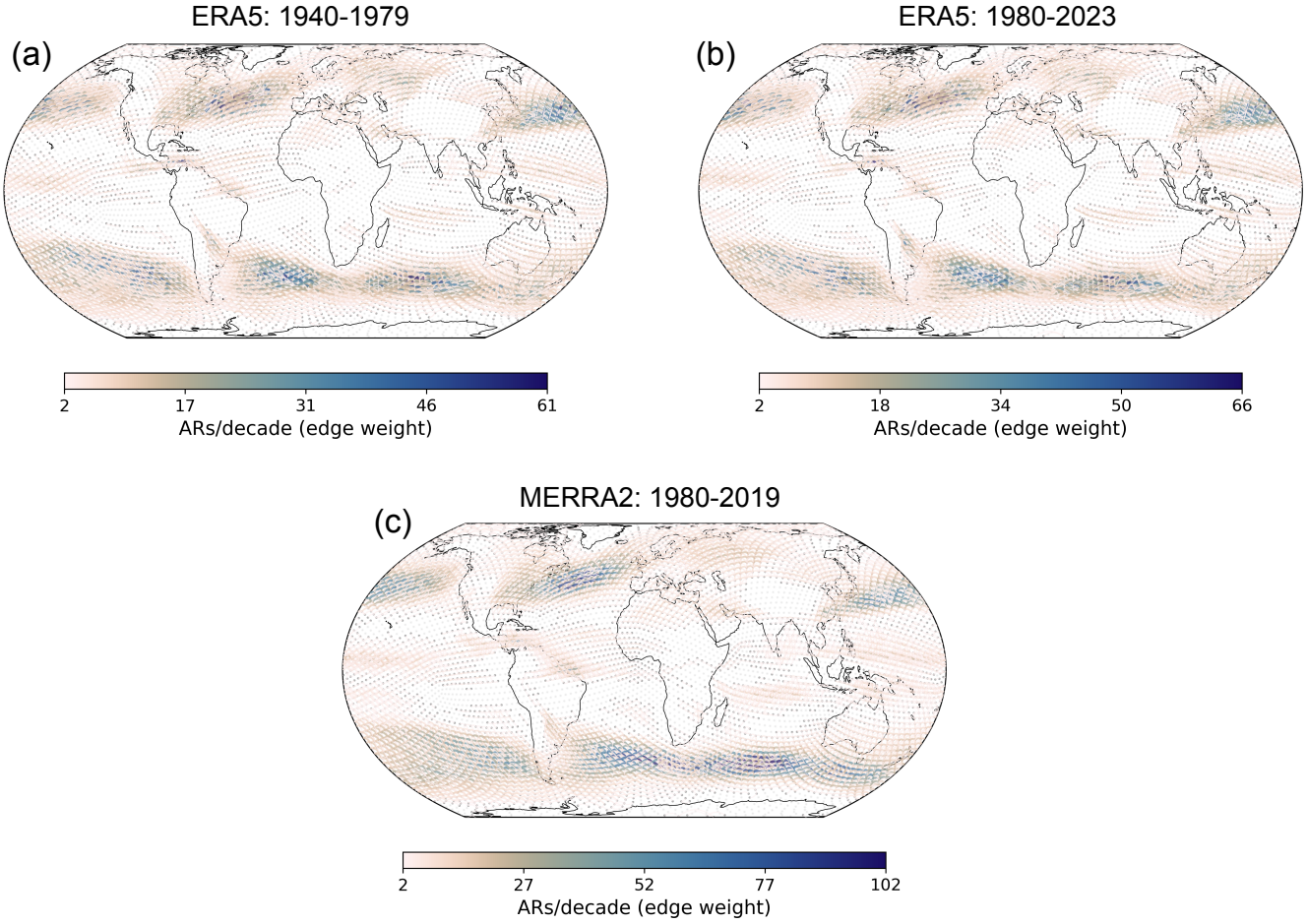

Figure S1. AR consensus network computed from (a) pre-1980 ERA5, (b) post-1980 ERA5, and (c) MERRA2. Edge weights are scaled logarithmically with $\epsilon = 2$ARs/decade. Overall, the main large-scale transport patterns are recovered across all three datasets. The MERRA2-based AR network yields transport frequencies twice as high as those for ERA5 as AR trajectories have 3h- instead of 6h-resolution. While pre-1979 ERA5 is known to suffer from observational biases, the general global structure of the AR network remains robust.

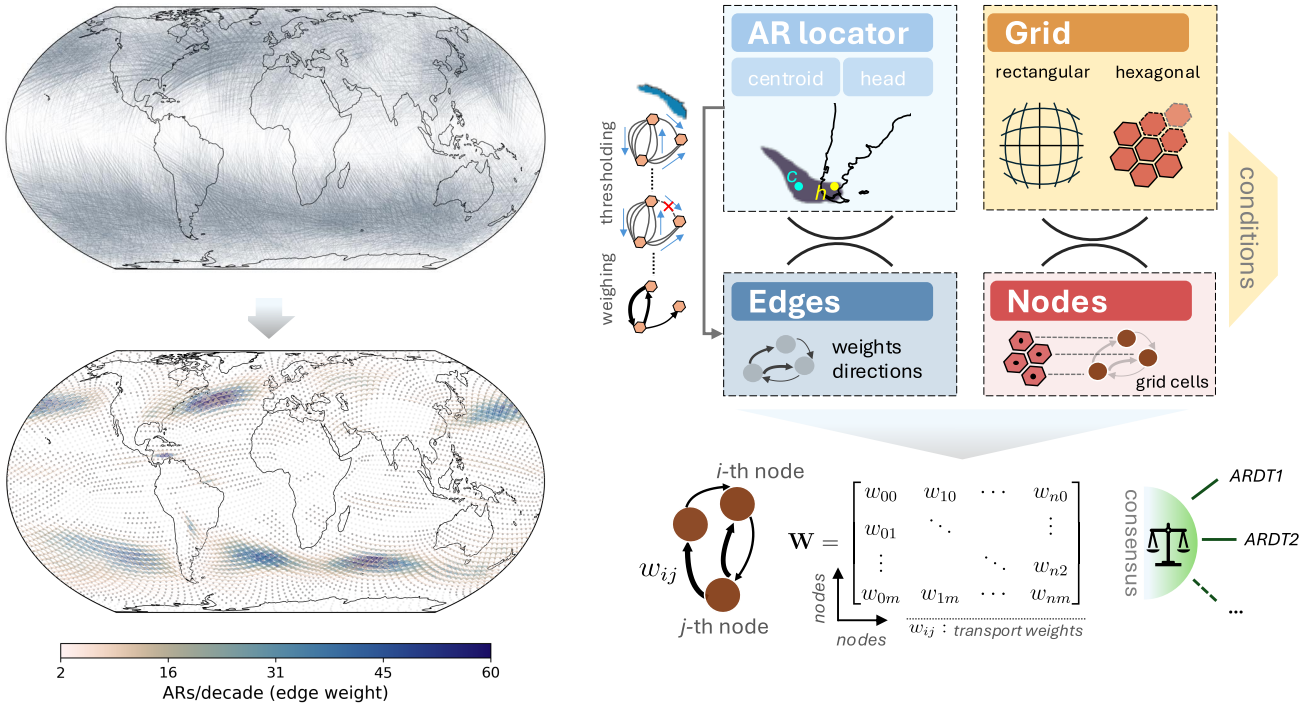

Figure S2. Schematic illustration of how an AR network is generated from an ensemble of AR trajectories, i.e., Lagrangian data from one (or multiple) AR catalogs. ARs are represented by a single 2-dimensional locator, e.g., their centroids or heads. AR trajectories are sequences of grid cells traversed by this locator. The grid can be defined as a conventional rectangular grid or a hexagonal grid to reduce spherical distortions. Edges are directed and weighted, denoting how frequently and into which directions AR move from a given node. This defines the (asymmetric) transport matrix $\mathbf{W}$ in which each element stores the transport frequency from node n to node m. The transport matrix can be thresholded and defines the AR network as its adjacency matrix. Given a set of different AR catalogs, an adjacency matrix can be derived from each catalog individually and a consensus derivation yields the consensus network.

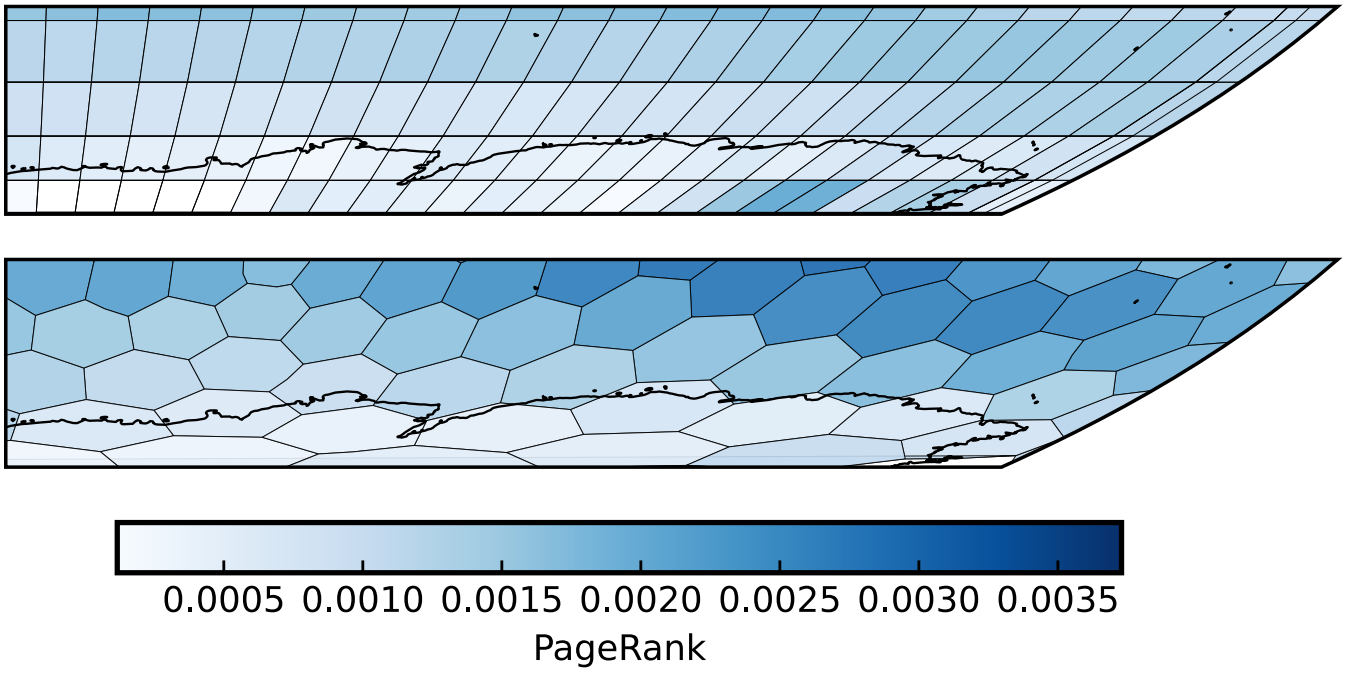

Figure S3. PageRank scores over east Antarctica, derived from a network on a rectangular (top) and a hexagonal (bottom) grid using an equal area projection. Grid cell sizes are selected to cover similar total areas. Towards the poles, rectangular grid cells get distorted more significantly and individual cells cover smaller and smaller areas. On the other hand, the number of hexagonal grid cells significantly shrinks towards the poles, approximately recovering equal areas over each grid cell. Rectangular grid overestimate node importance for nodes that are placed at high latitude grid cells (here given by PageRank scores): for the rectangular grid, two nodes over interior east Antarctica overprint the spatial variability in PageRank scores while for the hexagonal grid, less nodes over interior east Antarctica yield lower PageRank scores and reveal more continuous variability of node importance over the displayed region.

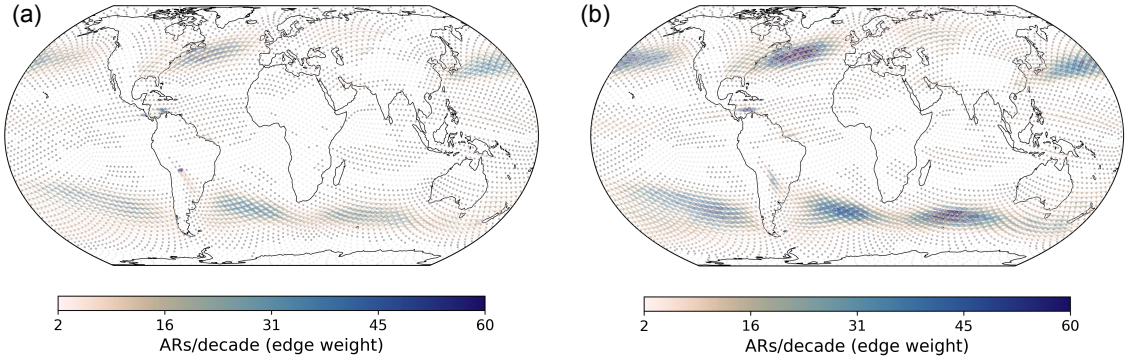

Figure S4. AR network from the PIKART-1 catalog with ARs located by their cores (a) as compared to their centroids (b) with $\epsilon = 2$ARs/decade. The AR core is the location with highest integrated vapor transport over an AR's contours. It marks a location that is potentially conducive of precipitation. While core trajectories appear less spatially centralized, the overall structures of the core-based and centroid-based AR networks align well.

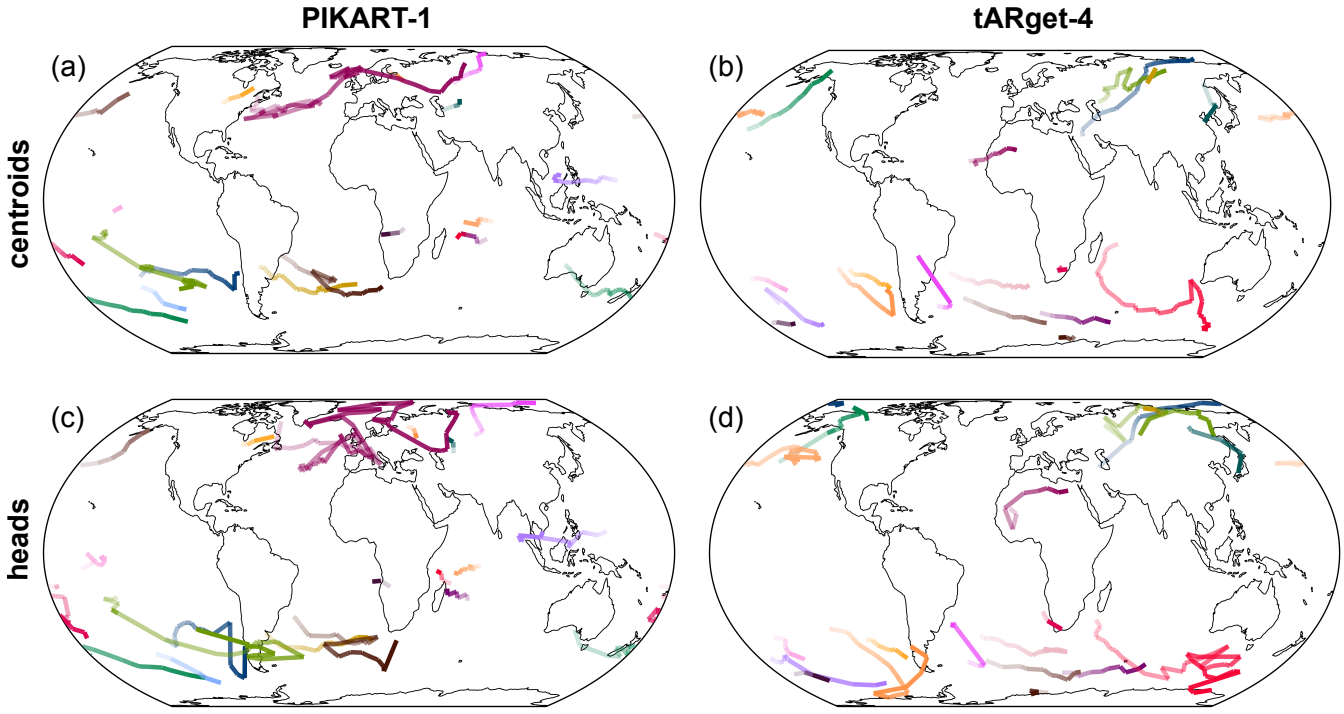

Figure S5. Examples of AR trajectories for AR centroids (a)/(b) and AR heads (c)/(d). The 20 displayed AR trajectories have been randomly selected from, (a)/(c) the PIKART-1 catalog, (b)/(d) the tARget-4 catalog. The individual trajectories are drawn from random time instances. They are, however, consistent between the respective AR 'centroid' and 'head' panel. Individual AR trajectories, e.g., the darkred PIKART trajectory over the United Kingdom ((a)/(b)), can linger within a confined spatial region for several steps. During such a period, ARs may reside over the same location, e.g., due to orographic barriers, but due to deformations, the AR centroid/head still move. AR heads are spatially displaced from AR centroids, usually showing a more northwesterly/southwesterly tendency in the NH/SH extratropics, respectively. Their motion yields more erratic trajectories, indicating that AR head locations are more susceptible to AR deformations than AR centroids.

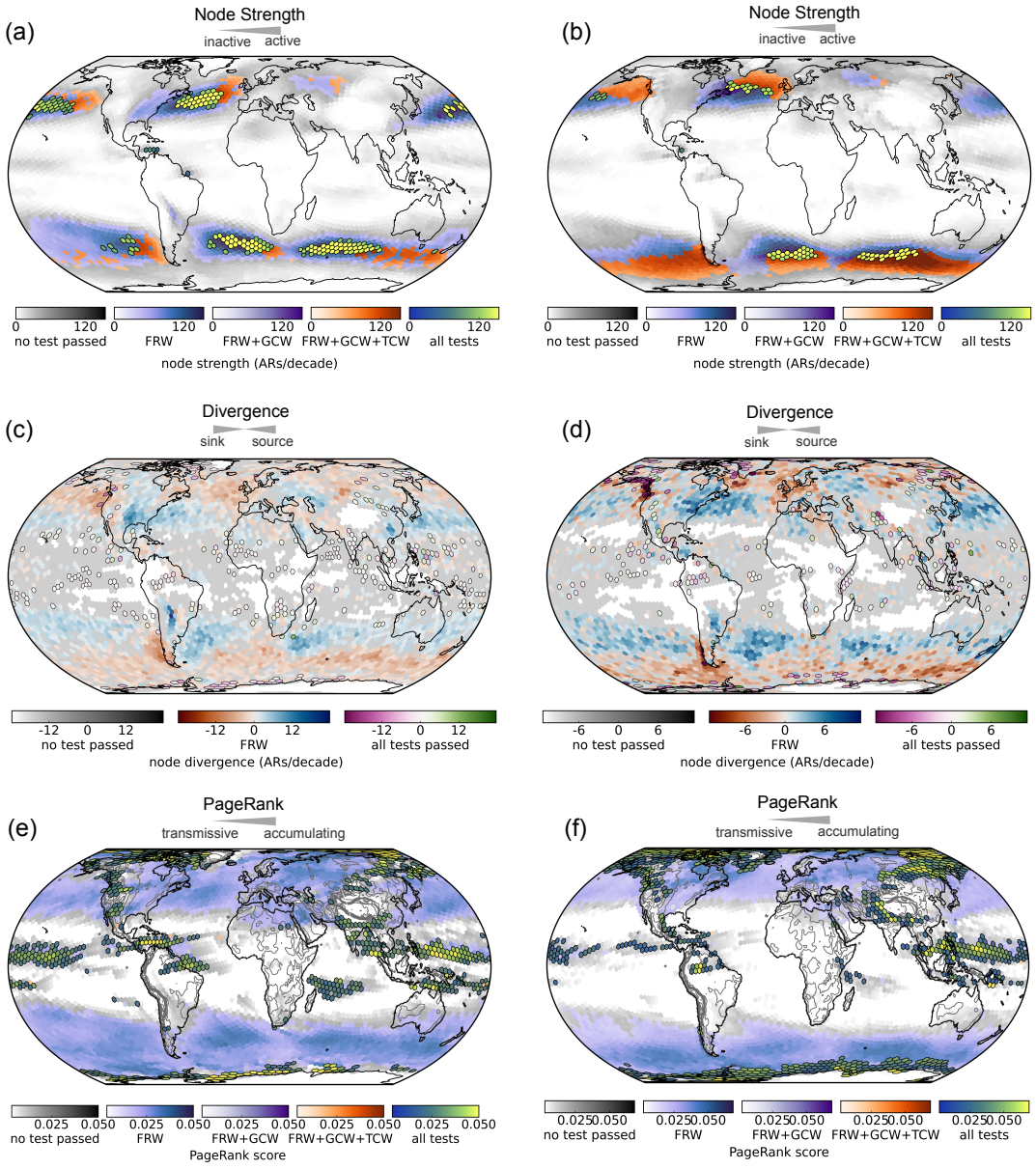

Figure S6. AR hubs, captured by node strength (a)/(b), node divergence (c)/(d) and PageRank (e)/(f) for ARs located by their centroids (a)/(c)/(e) and heads (b)/(d)/(f). (a)/(b) Node strength of each node in the AR centroid/head network, tested against all null models in an aggregated fashion. (c)/(d) Divergence score of each node in the AR centroid/head network, tested against the FRW and all null models. (e)/(f) PageRank score (normalized to % of total accumulated 'AR walker mass') of each node in the AR centroid/head network. The distinct colour maps in each panel indicate which set of tests was passed while still showing continuous variations of the respective network metric.

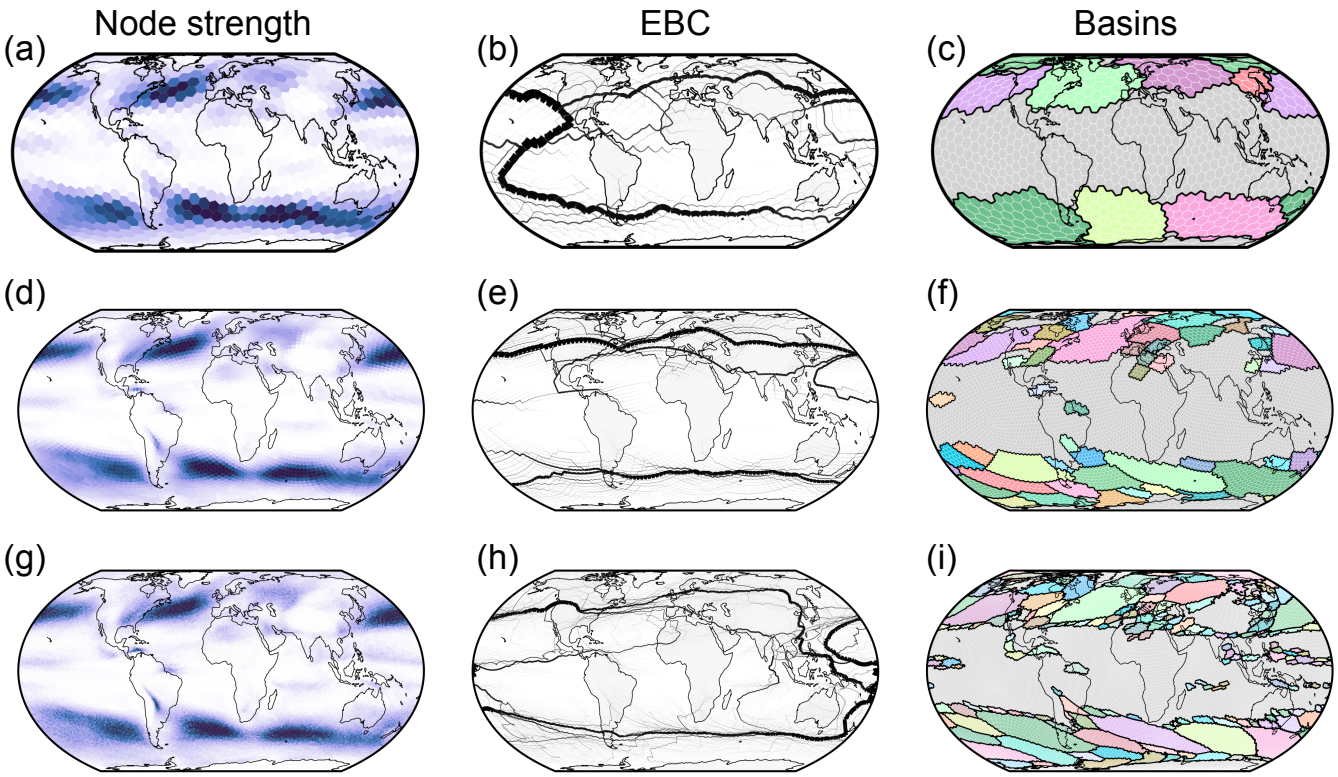

Figure S7. Sensitivity of ARTN analyses to spatial resolution. Node Strength (a/d/g), edge betweenness centrality EBC (b/e/h) and AR basins (c/f/i) for three different hexagonal grid cell sizes (rows, from top to bottom: $\approx 7.0^\circ$, $\approx 2.65^\circ$ and $\approx 1.0^\circ$ at the equator). The results generally depend on the combination of the spatial resolution and the threshold parameter ϵ. Here, ϵ was chosen heuristically such that global link densities match approximately.

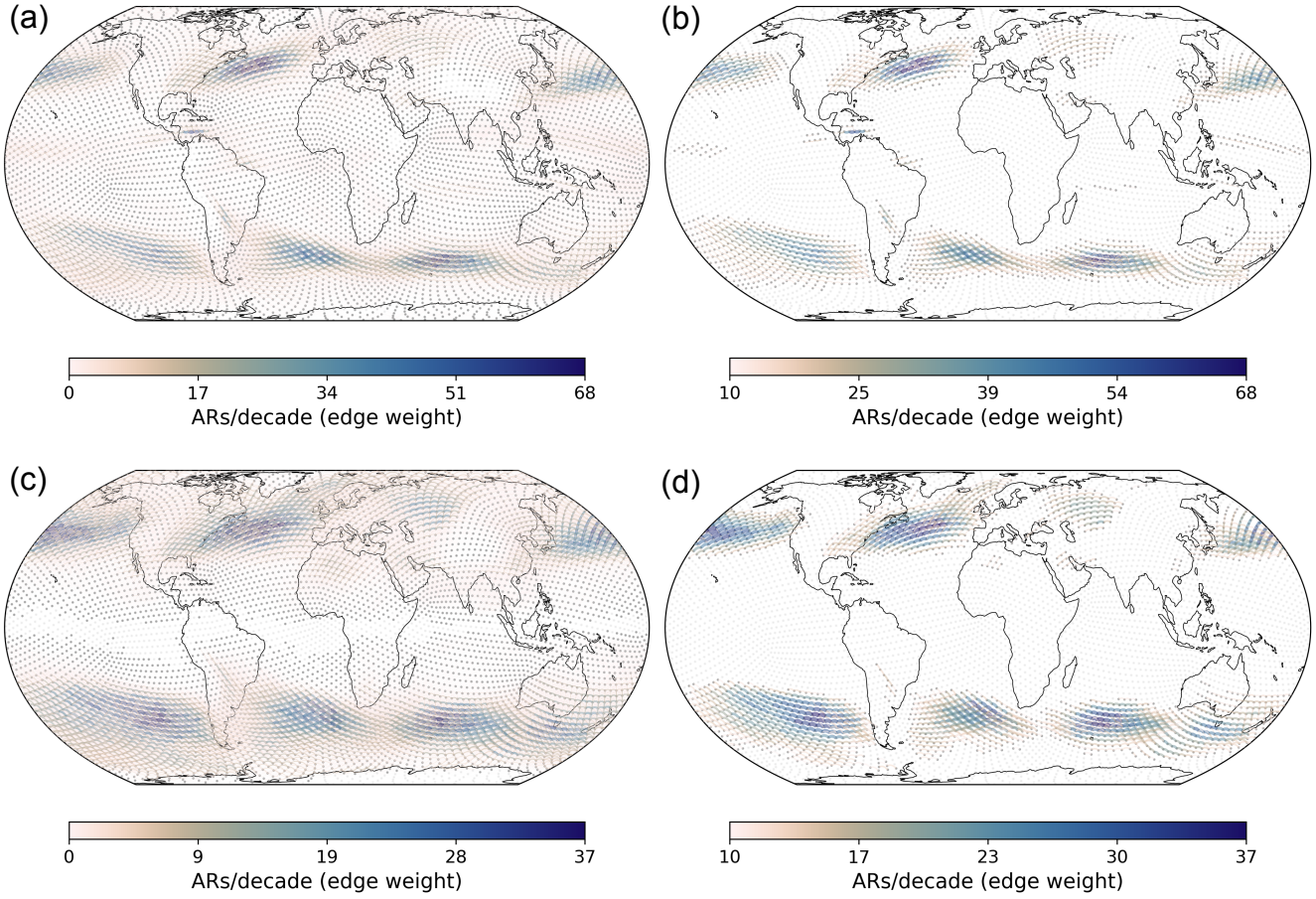

Figure S8. AR networks for different thresholds. No thresholding is applied in panel (a) and (c) for the AR networks derived from the PIKART and the tARget-4 catalog, respectively. This gives rise to a high number of edges with low AR frequency. Conversely, thresholding with a relatively high minimum AR frequency of at least ten ARs per decade is applied in panel (b) and (d) for the AR networks derived from the PIKART and the tARget-4 catalog, respectively. The resulting networks are more disconnected and concentrated around the main transport bands.

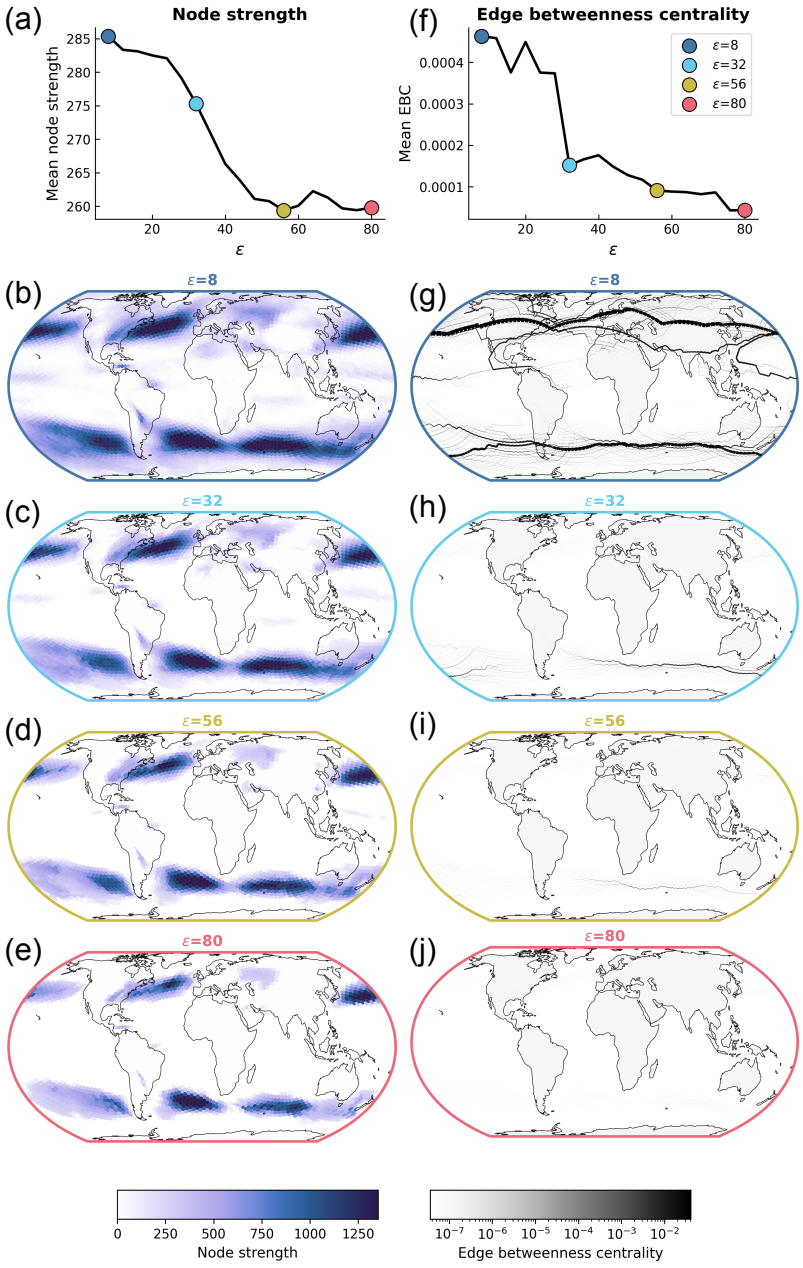

Figure S9. AR network metrics for different thresholds in the consensus network from the PIKART and the tARget-4 catalog. Node strength (left, (a)-(e)) and edge betweenness centrality (right, (f)-(j)) for varying thresholds ϵ. Continuous variations of ϵ are displayed in (a)/(f). As the network disconnects, regions of enhanced node strength shrink concentrically and edges with high EBC disappear, disrupting AR highways.

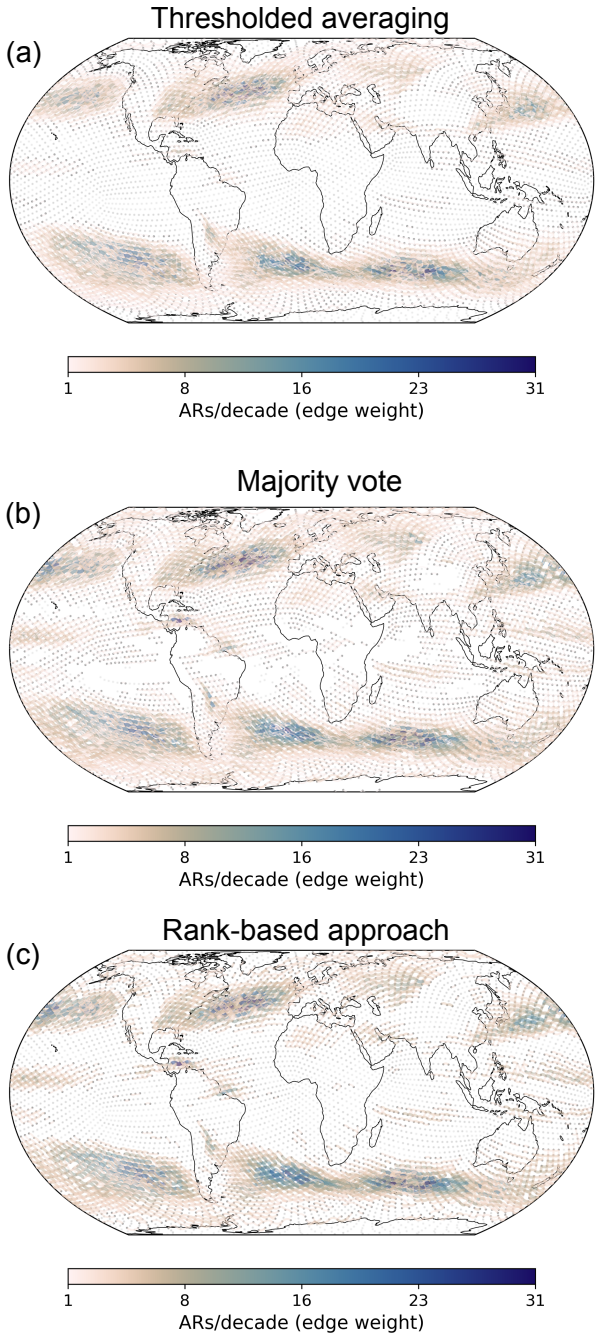

Figure S10. Different consensus formation approaches for integrating multiple AR catalogs into a single AR network. (a) Threshold averaging approach is the default approach used in the manuscript. (b) Majority votes compute the median edge weight from edges that are present in at least 75% of the considered AR catalogs. (c) Rank-based votes are derived by replacing edge weights by their percentile rank [0, 1] across all edges in that network. An edge survives if its mean rank (over all networks that cover this area) exceeds ϵ.

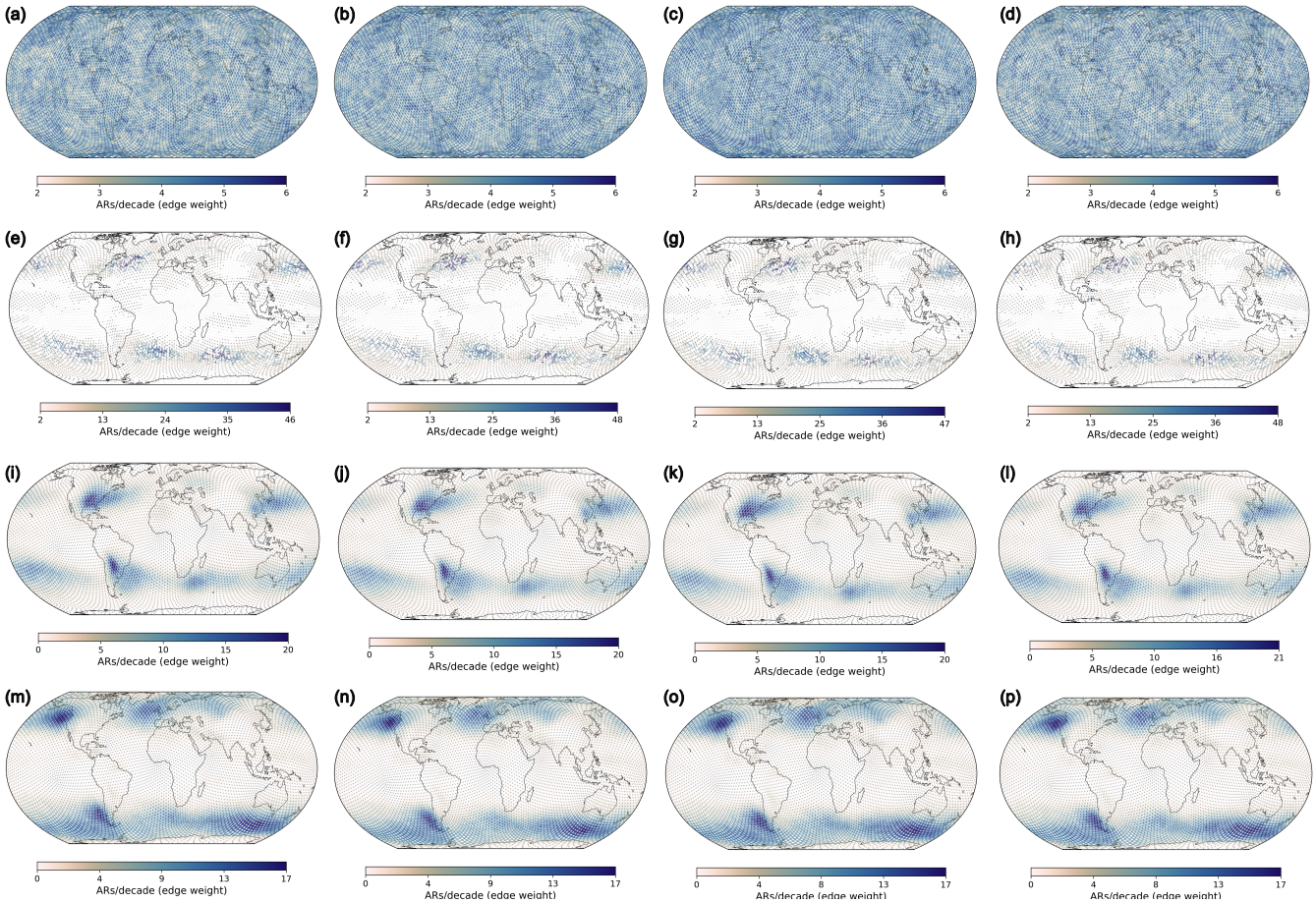

Figure S11. Four example realizations of each null model. (a)-(d) FRW model, (e)-(h) RWG model, (i)-(l) GCW model, (m)-(p) TCW model. All models visibly recover the constrained features, i.e., local connectivity in the RWG model ((e)-(h)), AR genesis regions in the GCW model ((i)-(l)), and AR termination regions in the TCW model ((m)-(p)). The FRW model ((a)-(d)) only constrains the number of AR trajectories and their lifetimes but clearly generates networks with random spatial structure. Differences between the realization solely arise from the stochastic, unconstrained components of the models and can be seen upon closer visual inspection of each network's small-scale connectivity.

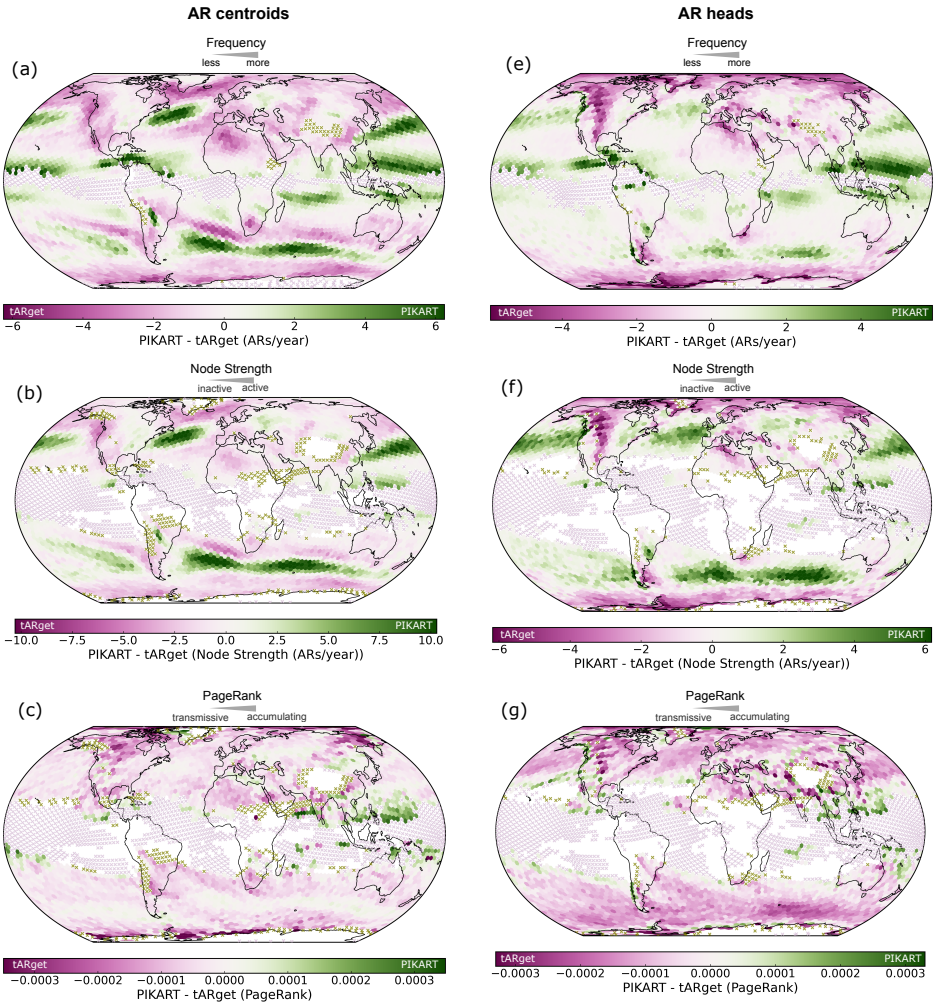

Figure S12. Comparison between node importance in PIKART-1 and tARget-4. All panels show differences between a property derived from the PIKART-1 catalog to those derived from the tARget-4 catalog at each location. The left column (a)-(c) locates ARs by their centroids, the right column (d)-(f) by their heads. Green (pink) colors denote higher importance in PIKART-1 (tARget-4). Green (pink) crosses mark nodes where there are not sufficient ARs in the PIKART-1 (tARget-4) catalog. Independent of any AR networks, (a)/(d) show AR frequency differences across both catalogs. PIKART-1 tracks more ARs in the tropics, along the main transport basins and over parts of interior South America. tARget-4 exhibits enhanced AR frequencies at the poles, over interior North America and other continental regions, e.g., North Africa. Differences in node importance based on node strength (b)/(e) largely align with these patterns. Nodes with crosses in (b)/(e) and no crosses in (a)/(d) arise due to thresholding of the network. Differences in node importance based on PageRank scores (c)/(f) show that tARget-4 assigns higher PageRanks to most nodes, except for tropical regions (for AR centroids and heads) and some coastal regions such as western North American, Chile, Greenland and Antarctica for AR heads.

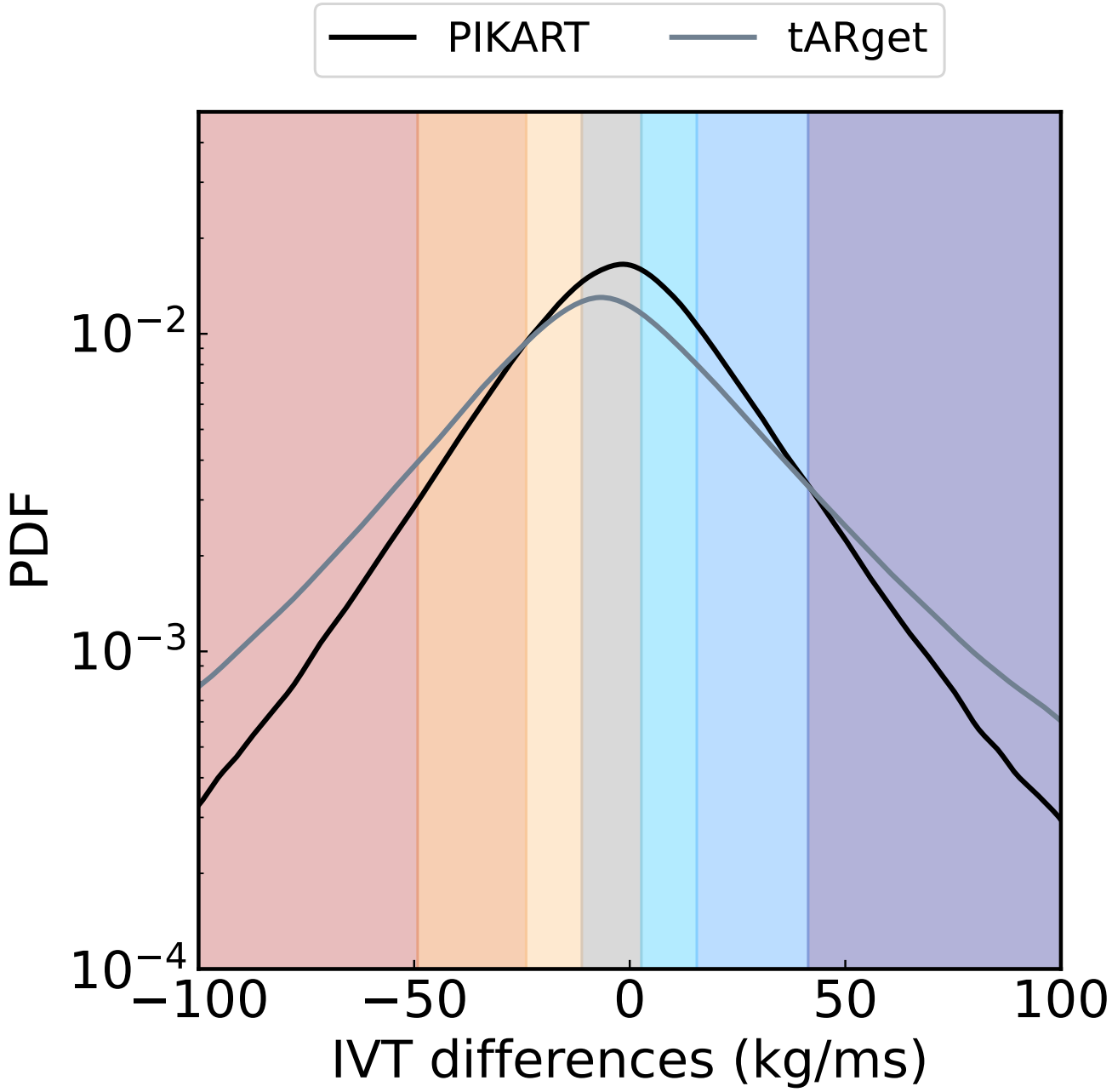

Figure S13. Kernel density estimate of log-probability density functions of differences in integrated vapor transport. Differences are computed between each pair of consecutive AR steps for each of the two catalogs. Colored shading highlights the corresponding thresholds used for discretization of IVT differences (10%, 25%, 40%, 60%, 75%, 90% quantiles derived from IVT differences in both catalogs together, from left to right). Red denotes large IVT losses and blue denotes large IVT gains. IVT losses and gains can be both caused by changes in wind speed and relative humidity.

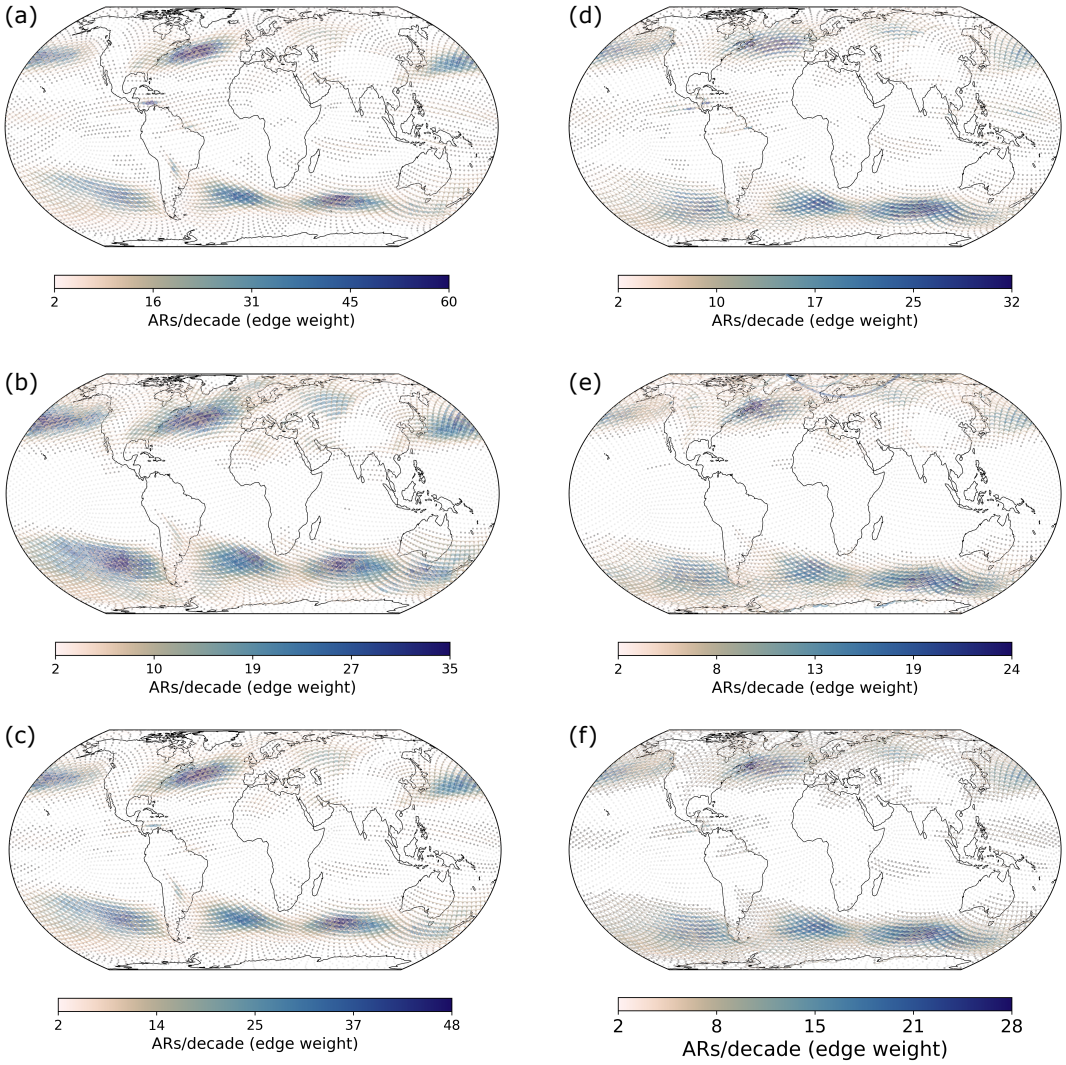

Figure S14. AR network from each catalog and the consensus network (with AR centroids and heads). Networks are derived from, (a)/(d) the PIKART-1 catalog and (b)/(e) the tARget-4 catalog with $\epsilon = 2$ARs/decade. Consensus networks are shown in (c)/(f). AR locators are the AR centroid (a)-(c) and the AR head (d)/(f). The AR head marks a location that is more informative about AR inland penetration and potential AR-induced continental precipitation. All displayed head-based networks are shifted towards the interior of continents and the poles than their centroid-based counterparts.

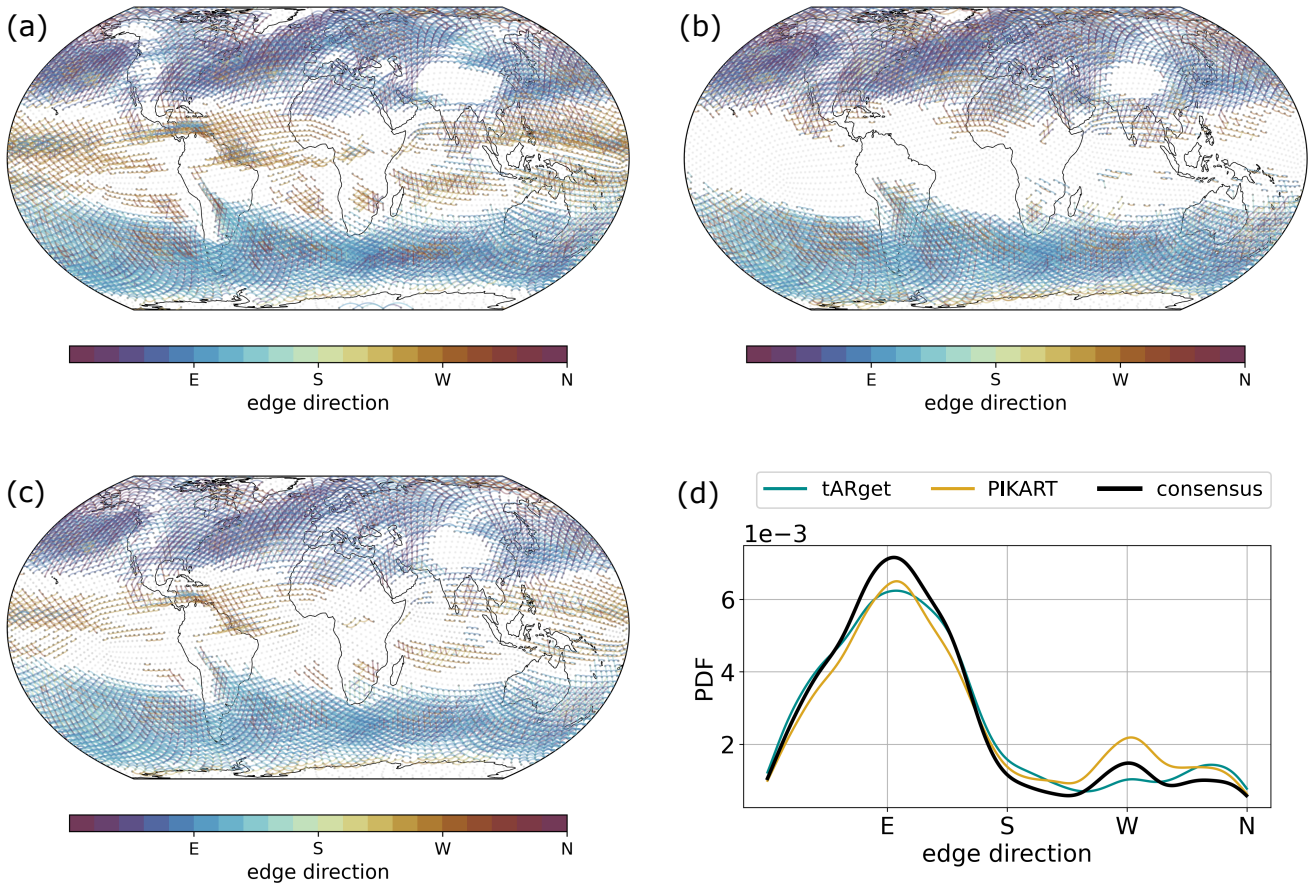

Figure S15. AR network from each catalog ((a)/(b) and the consensus network (c), colored by edge direction. Networks are derived from, (a) the PIKART catalog, (b) the tARget V4 catalog, (c) their synthesis by means of their consensus network with $\epsilon = 2$ARs/decade. Edges are predominately aligned with the westerlies in both extratropical hemispheres and deviate more poleward closer to the poles. In the (sub)tropics, edges tend towards the west. Edge directions are overall consistent between both catalogs and the consensus network (d). The largest deviation results from PIKART-1 tracking ARs in the (sub)tropics more permissively than tARget-4, giving rise to a larger population of westward directed edges.

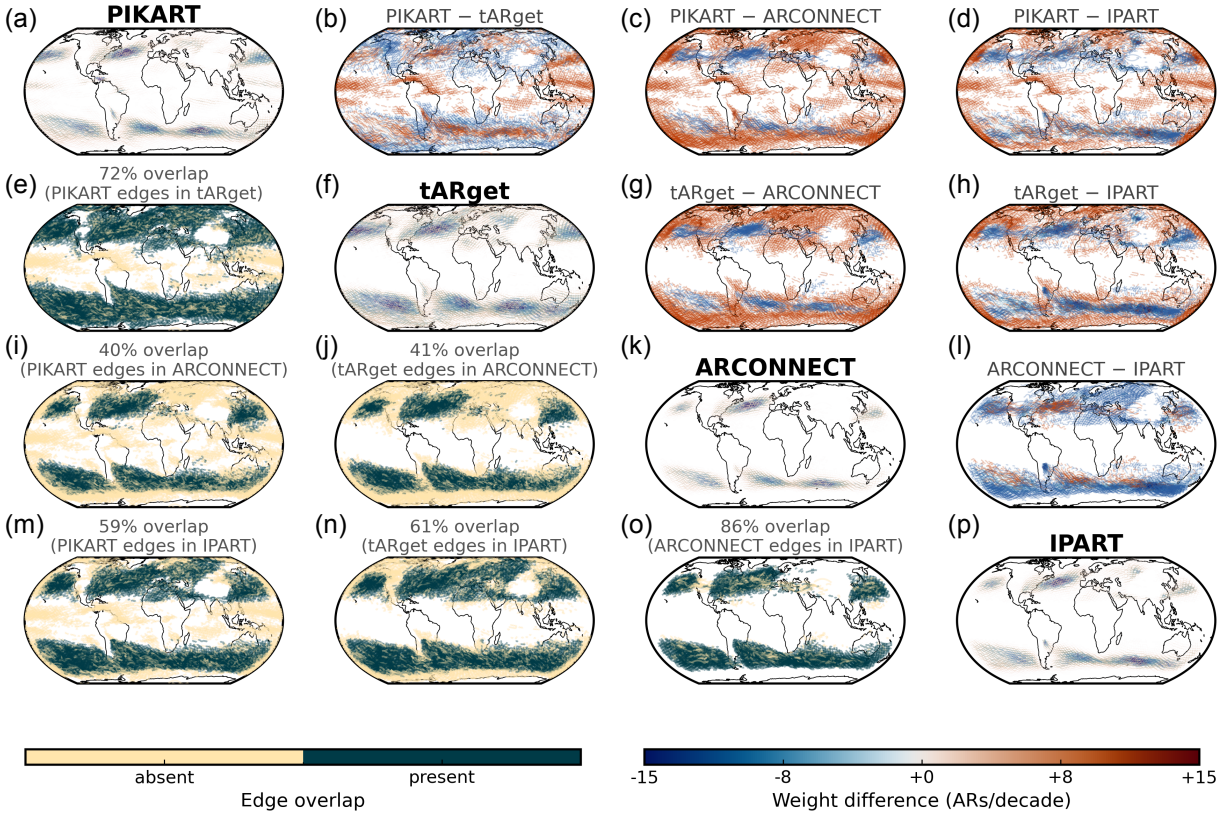

Figure S16. AR networks derived from PIKART-1, tARget-4, ARCONNECT and IPART-1 and their agreement. Diagonal plots ((a)/(f)/(k)/(p)) show individual networks. Plots in the lower triangular ((e)/(i)/(j)/(m)/(n)/(o)) show whether a given edge is present in both networks. Global edge overlap is given in the titles. Plots in the upper triangular ((b)/(c)/(d)/(g)/(h)/(l)) show the pairwise difference in edge weights.

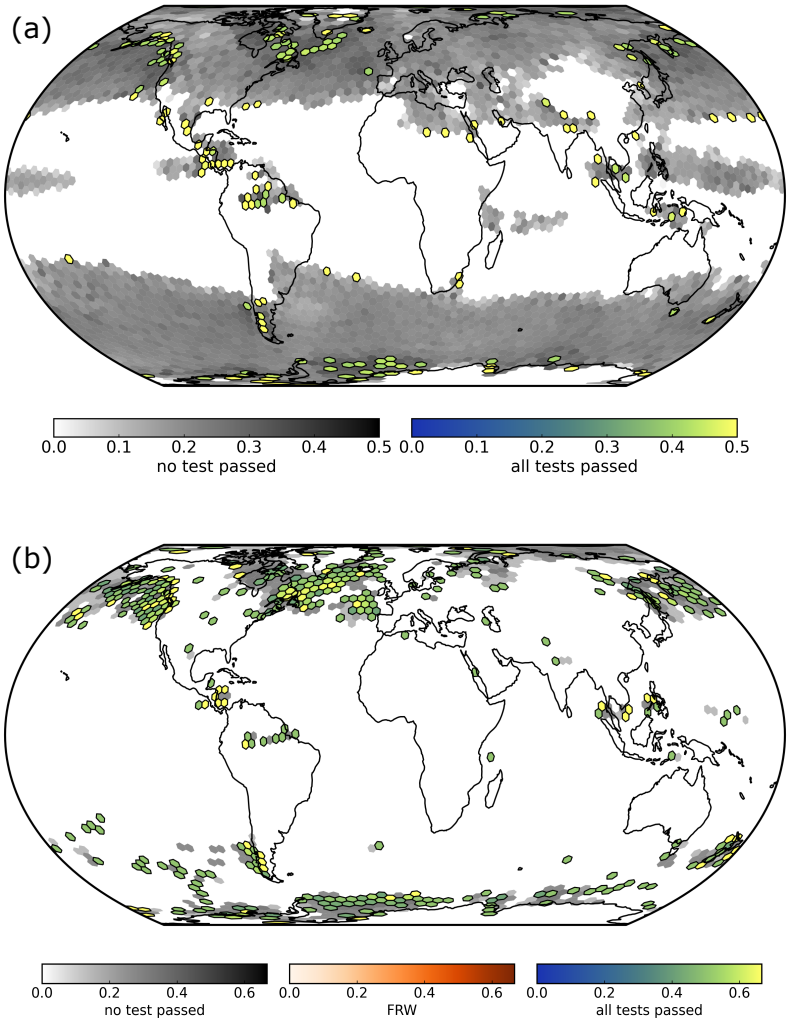

Figure S17. Clustering coefficients for the AR consensus network. (a) Regular clustering coefficients, highlighting regions where ARs tend to take various routes into all directions, resulting in closed triangles in the AR network. (b) Cycle clustering coefficient, i.e., fraction of closed triangles that form directed cycles in the AR network. Cycle clustering coefficients highlight regions where ARs may exhibit circular movement, e.g., in regions where they reside for prolonged time periods due to enhanced topography or where AR transport is dense along main transport corridors. The distinct colour maps in each panel indicate which set of tests was passed while still showing continuous variations of the respective network metric.

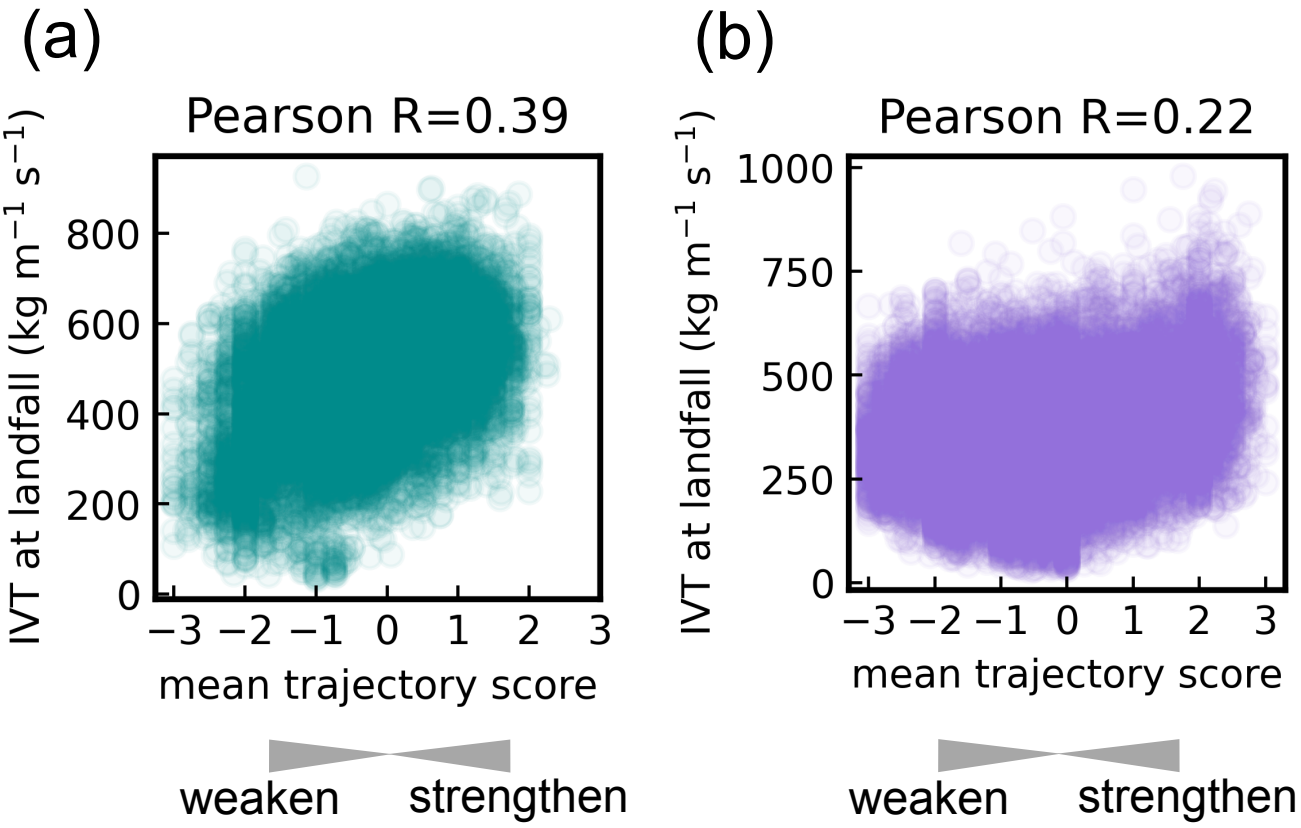

Figure S18. Scatter plots of mean trajectory score (based on IVT differences) versus IVT at landfall for both catalogs. First, discretized IVT difference values (between -3 and 3) have been assigned to each node in the ARTN (Fig. SS16). For each AR that lives longer than 18hrs, the trajectory score is computed as the average of all IVT difference scores it encounters during its lifecycle. These are predictive of IVT at landfall as ARs tend to intensify/weaken their IVT along their paths, resulting in the indicated statistically significant correlation values. The dependencies are shown separately for the (a) PIKART-1 and (b) tARget-4 catalog. The predictability scores shown in Fig. 2b of the main manuscript are derived from the residuals of a robust Huber regression through the displayed points, scaled by average of the indicated correlation values.

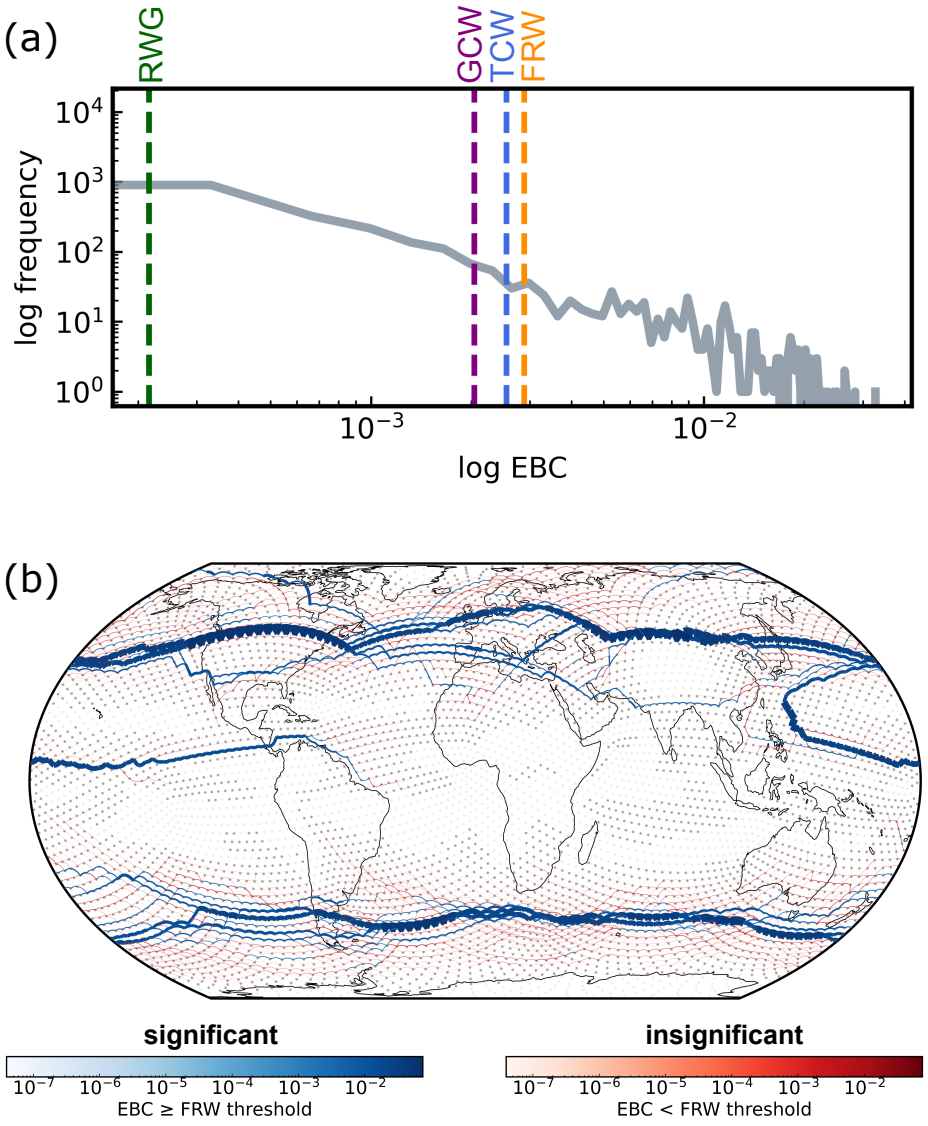

Figure S19. Significance testing of the identified global AR highways. (a) Histogram of edge betweenness centralities from (unconditioned) real consensus network with $\epsilon = 2$ARs/decade (log-log-scale). The upper 90%-quantiles for each null model ensemble (based on 200 model realizations) are shown as colored dashed lines. (b) If thresholded by the highest of these quantiles (FRW model), the main AR highways remain significant.

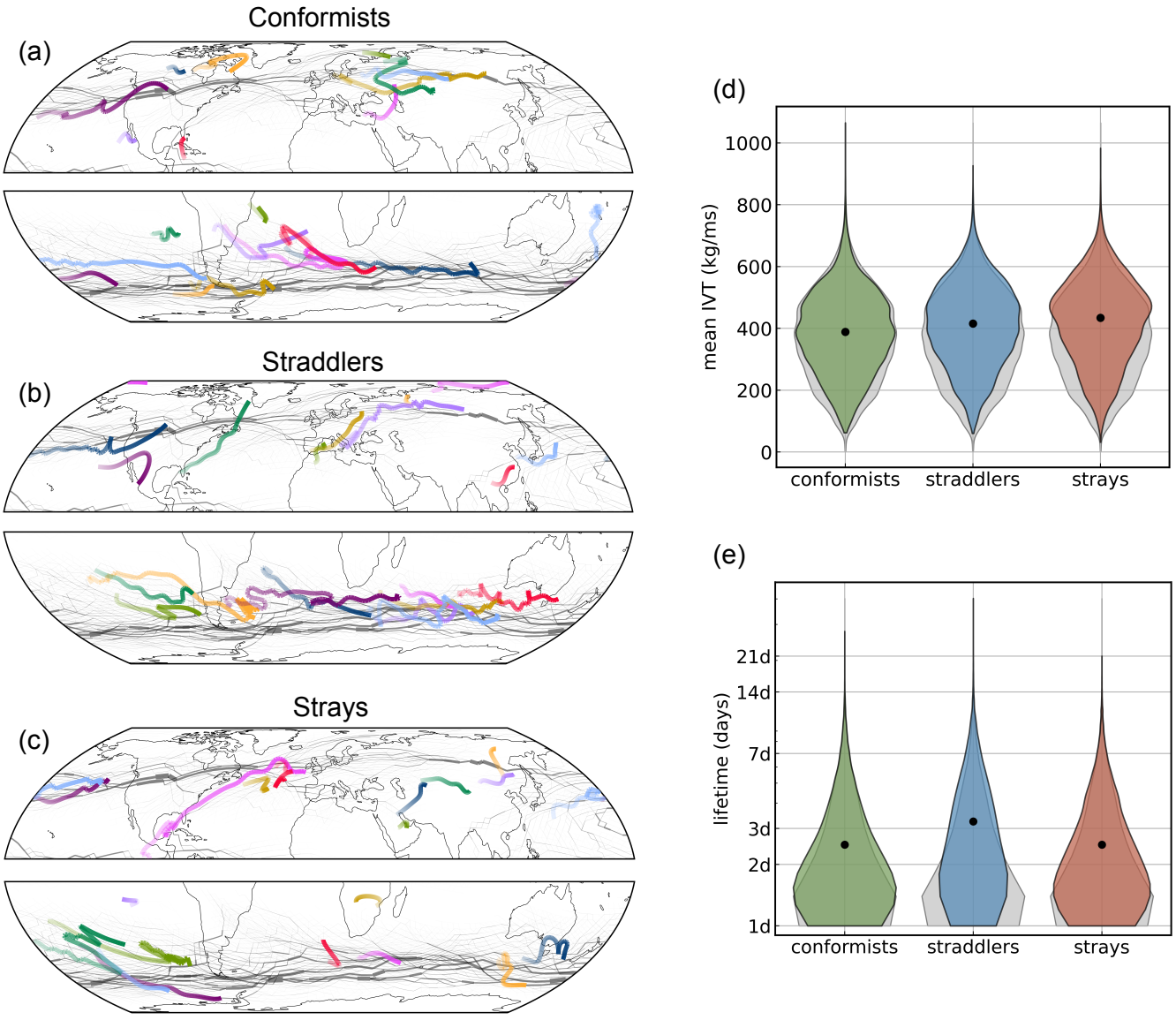

Figure S20. Trajectories of three AR populations that exhibit different tendencies in following the identified boreal winter (DJF) AR highways. (a) Trajectories of ten randomly selected ARs that were classified as *Conformists* (top-33% highest EBC-trajectories), (b) same but for ARs that were classified as *Straddlers* (middle-33% highest EBC-trajectories), (c) same but for ARs that were classified as *Strays* (lowest-33% EBC-trajectories). Network edges (grey) are weighed by their EBC. Opacity indicates temporal progression. (d) IVT distribution of distinct AR populations. (e) Logarithmic lifetime distribution of distinct AR populations. In (d)/(e), the overall distribution is plotted in grey in the background for reference.

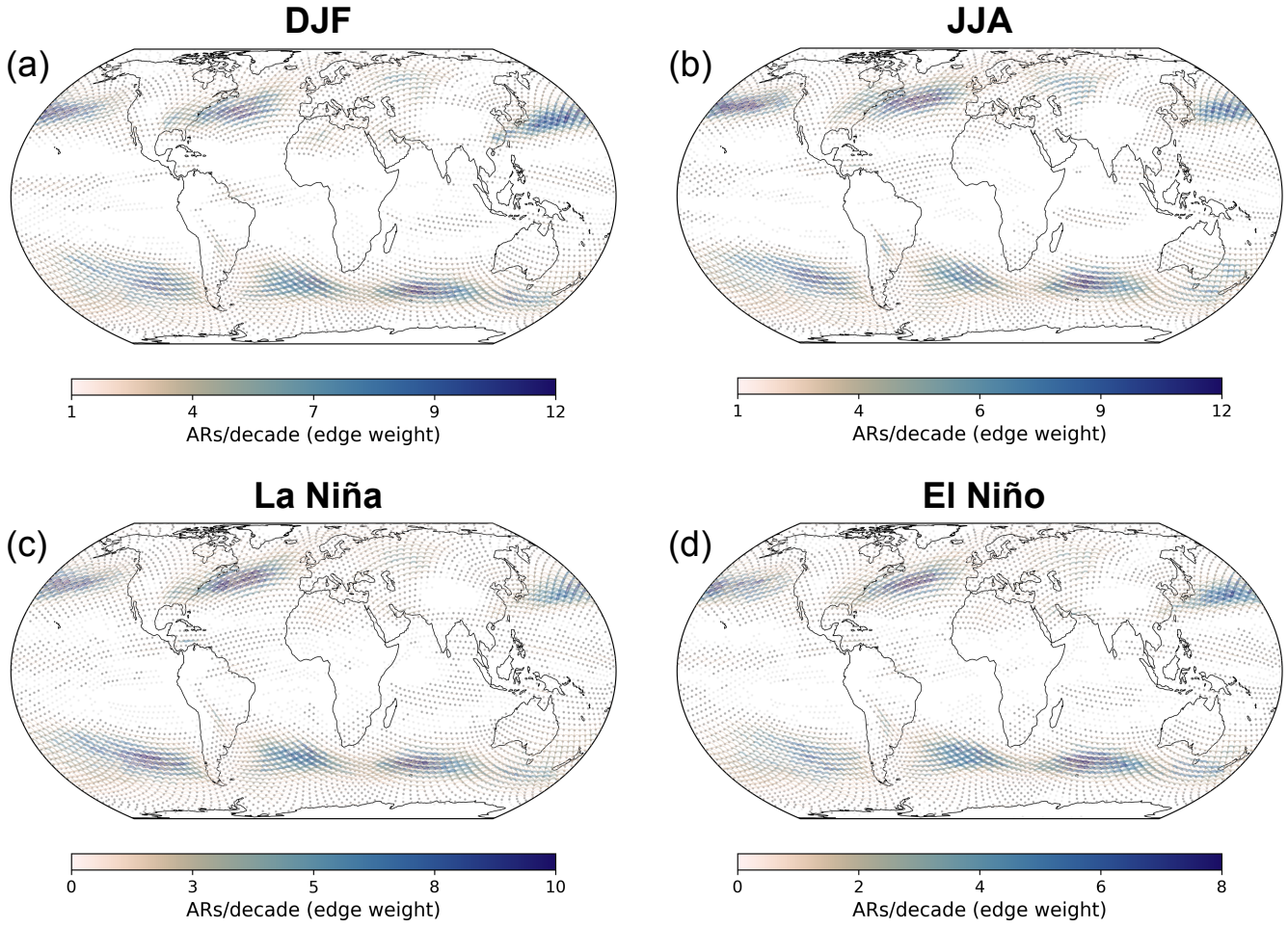

Figure S21. Conditional consensus networks. (a)/(b) AR networks conditioned on (a) boreal winter (DJF) and (b) summer (JJA). (c)/(d) AR networks conditioned on (a) La Niña and (b) EL Niño conditions.

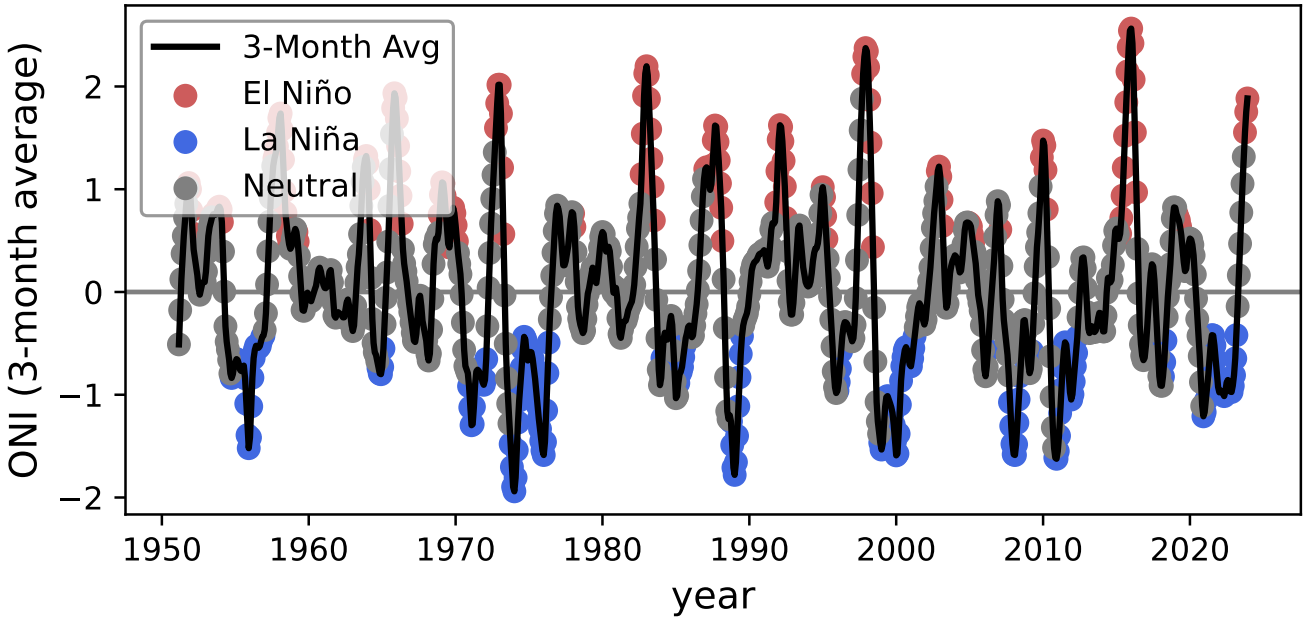

Figure S22. Moving average of Oceanic Niño Index (ONI) z-scores between 1950-2023. Grey dots denote neutral conditions. Red (blue) dots denote El Niño (La Niña) conditions, identified as excursions of at least five consecutive 3-months averages above 0.5 (below -0.5). The identified conditions are used to condition the AR network.

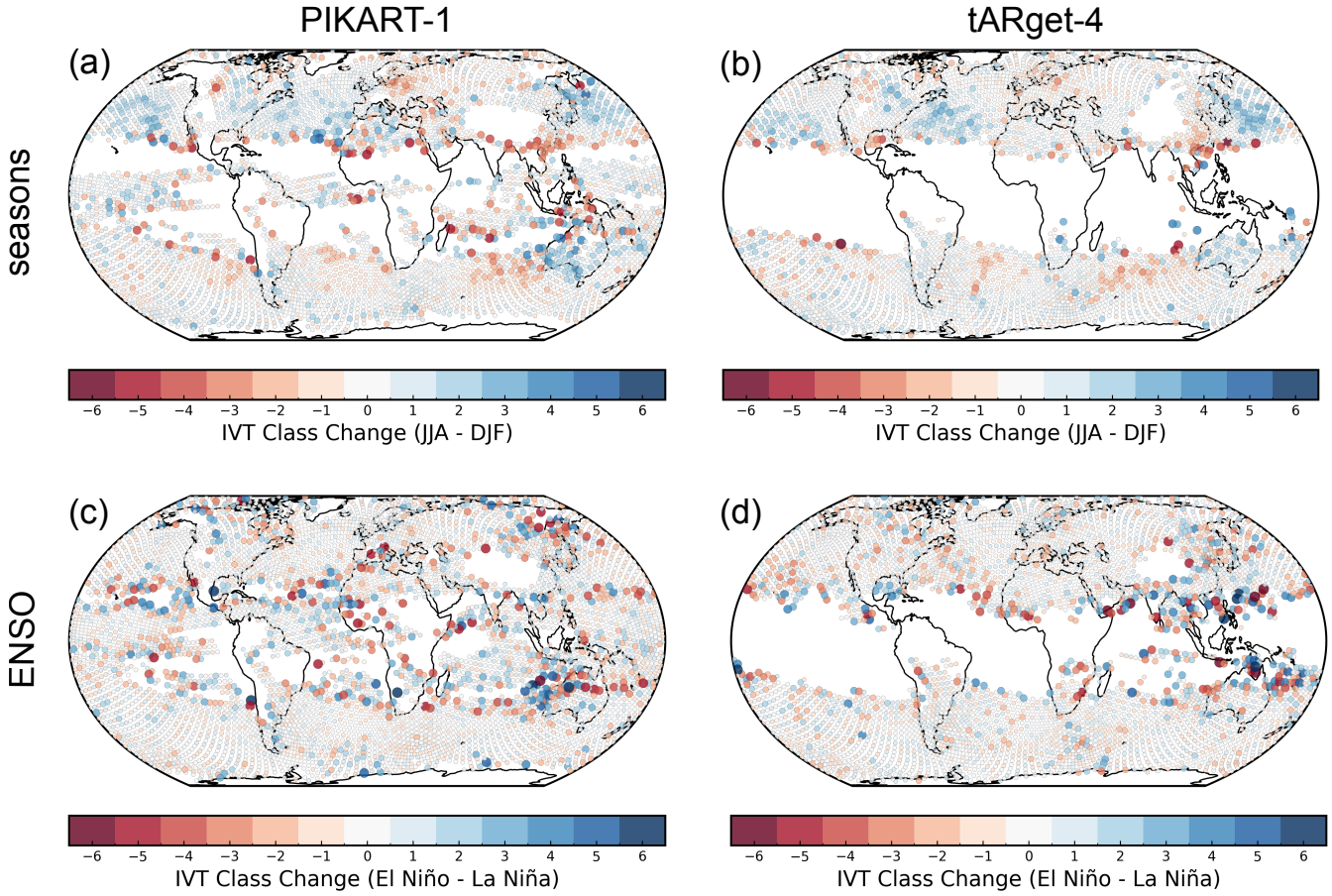

Figure S23. Differences between net IVT changes across nodes for seasonally end ENSO-conditioned AR networks. (a)/(b) Difference of discretized net IVT changes between boreal summer (JJA) and winter (DJF) for each node in the (a) PIKART-1 and (b) tARget-4 network. (c)/(d) Difference of discretized net IVT changes between El Niño and La Niña for each node in the (c) PIKART-1 and (d) tARget-4 network. As net IVT changes were discretized into seven classes (ranging from large losses (-3) to large gains (+3)), nodes can change their role in 13 ways (ranging from a change from large gains (+3) to large losses (-3), yielding -6, to a change from large losses (-3) to large gains (+3), yielding +6). Red bubbles denote nodes that become more of a sink (larger losses) during JJA or El Niño conditions, respectively. Blue bubbles denote nodes that become more of a source (larger gains) during JJA or El Niño conditions, respectively.

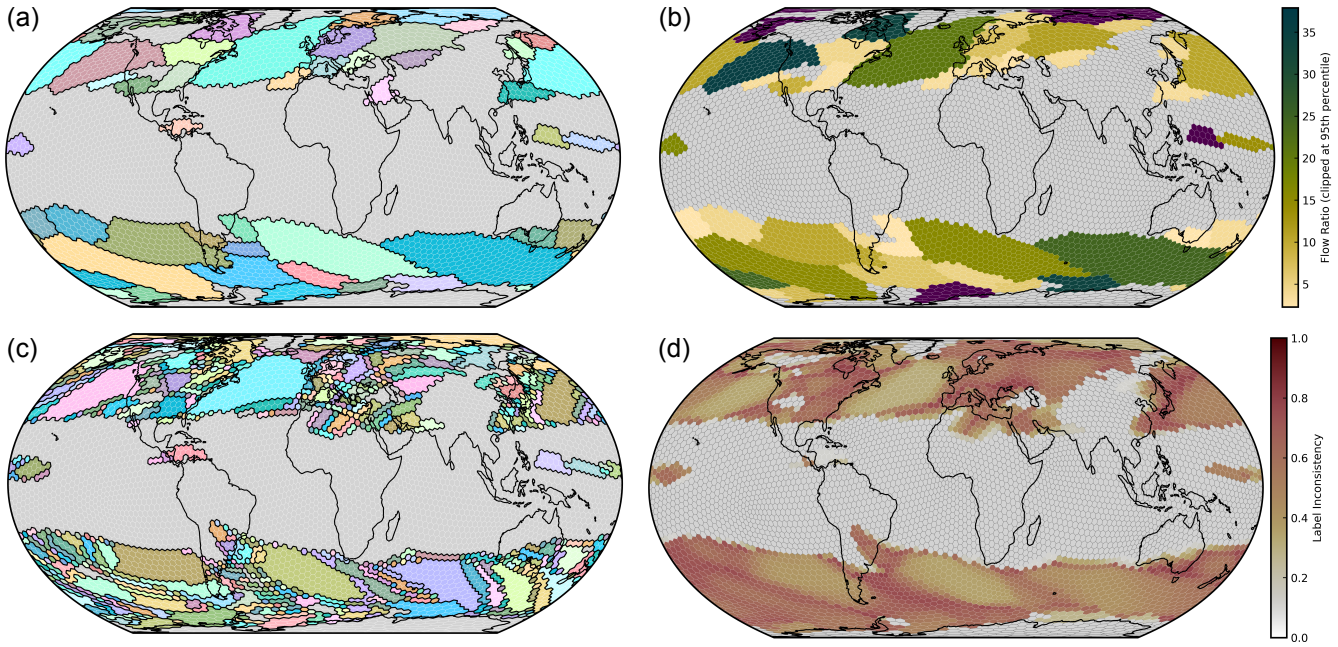

Figure S24. Stability and quality of AR basins identified through Infomap community detection on AR consensus network ($\epsilon = 1$**ARs/decade**). (a) Most central partition, defined as the set of communities that minimizes overall label incosistency across all nodes. (b) Flow ratios, indicating partition quality by means of intra- and inter-community flow. (c) Consensus partition, i.e., the most central community a node belongs to considering all of its distinct community labels across runs. (d) Label inconsistency, i.e., the heterogeneity of a node labels from all of its distinct community labels across runs. Both of the latter are computed from the Jaccard similarity between the different communities a node is assigned to across different runs. All measures are derived from 100 runs of the (non-hierarchical) Infomap algorithm, each seeded with a distinct random seed.

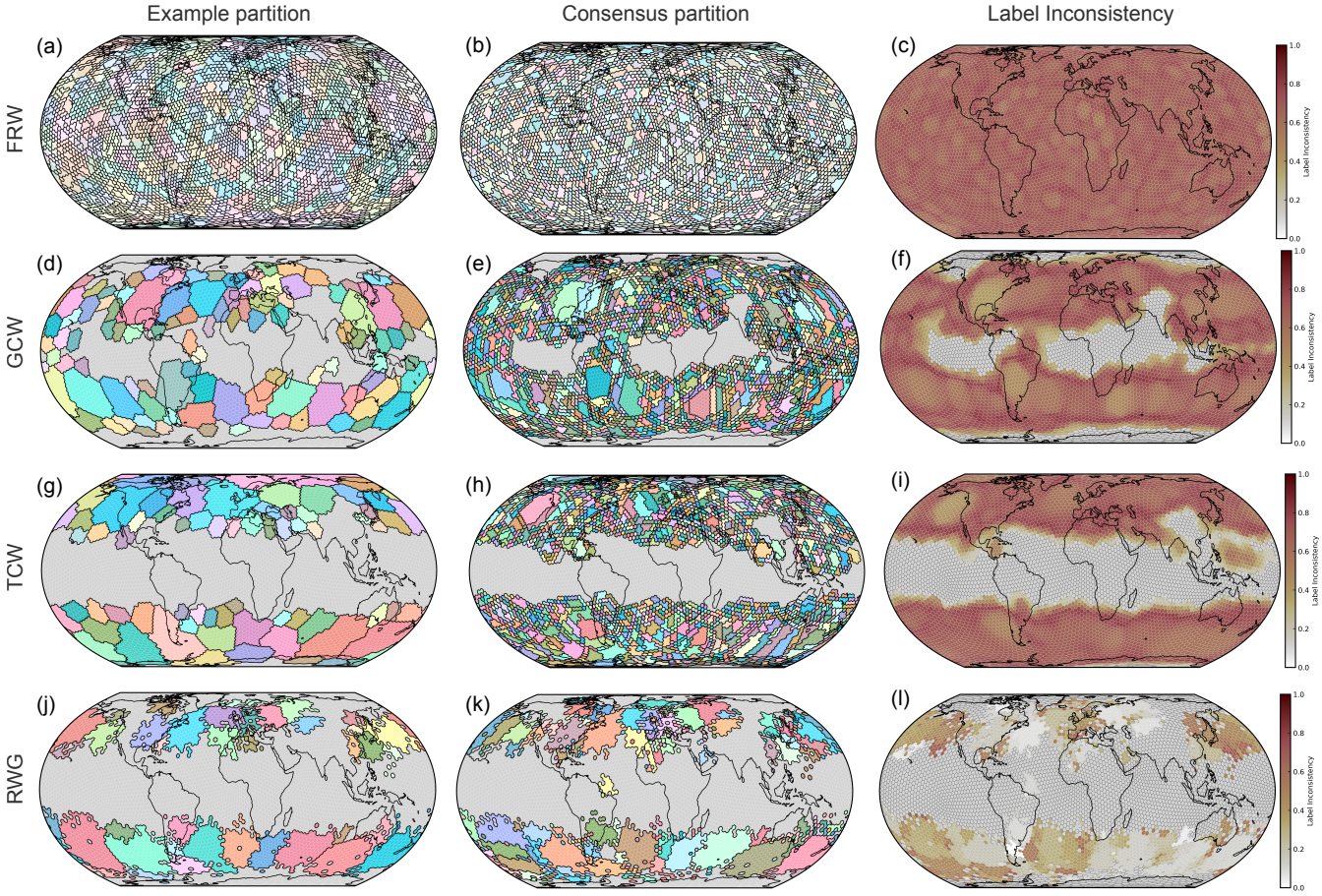

Figure S25. Stability and quality of AR basins identified through Infomap community detection on a single example realization of each of the null model networks ($\epsilon = 1$ARs/decade). Rows show output for distinct null models. (a)/(d)/(g)/(j) Selected example partition. (b)/(e)/(h)/(k) Consensus partition, i.e., the most central community a node belongs to considering all of its distinct community labels across runs. (c)/(f)/(i)/(l) Label inconsistency, i.e., the heterogeneity of a node labels from all of its distinct community labels across runs. Both of the latter are computed from the Jaccard similarity between the different communities a node is assigned to across different runs. All measures are derived from 100 runs of the (non-hierarchical) Infomap algorithm, each seeded with a distinct random seed.

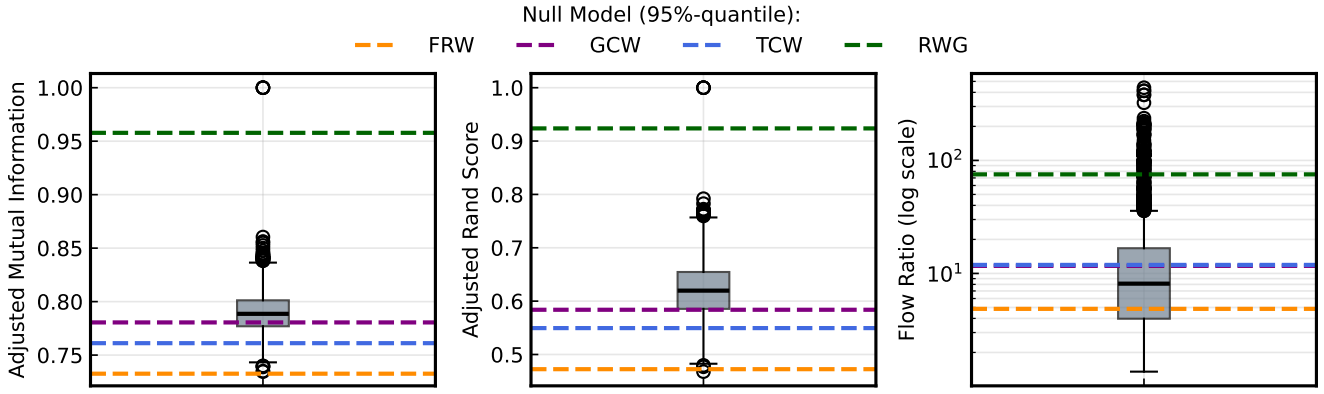

Figure S26. Significance testing of stability and quality of AR basins identified through Infomap community detection. Stability is measured through (a) Adjusted Mutual information and (b) Adjusted Rand Index. (c) Separation of communities is measured through flow ratios. The distribution of each metric is shown as a boxplot, providing the range of values observed for the communities identified across different runs of Infomap on the real AR consensus network. Horizontal dashed lines indicate the 95%-quantiles of all four null models. The real AR basins are consistently more stable and well-separated than expected from the FRW model (yellow line). The GCW and TCW model yield comparable stability and more well-separated communities as AR transport concentrates around genesis/termination hubs (blue/purple line). The RWG model yields very stable and well-separated communities, likely due to the hard constraint on local rewiring of nodes (green line).

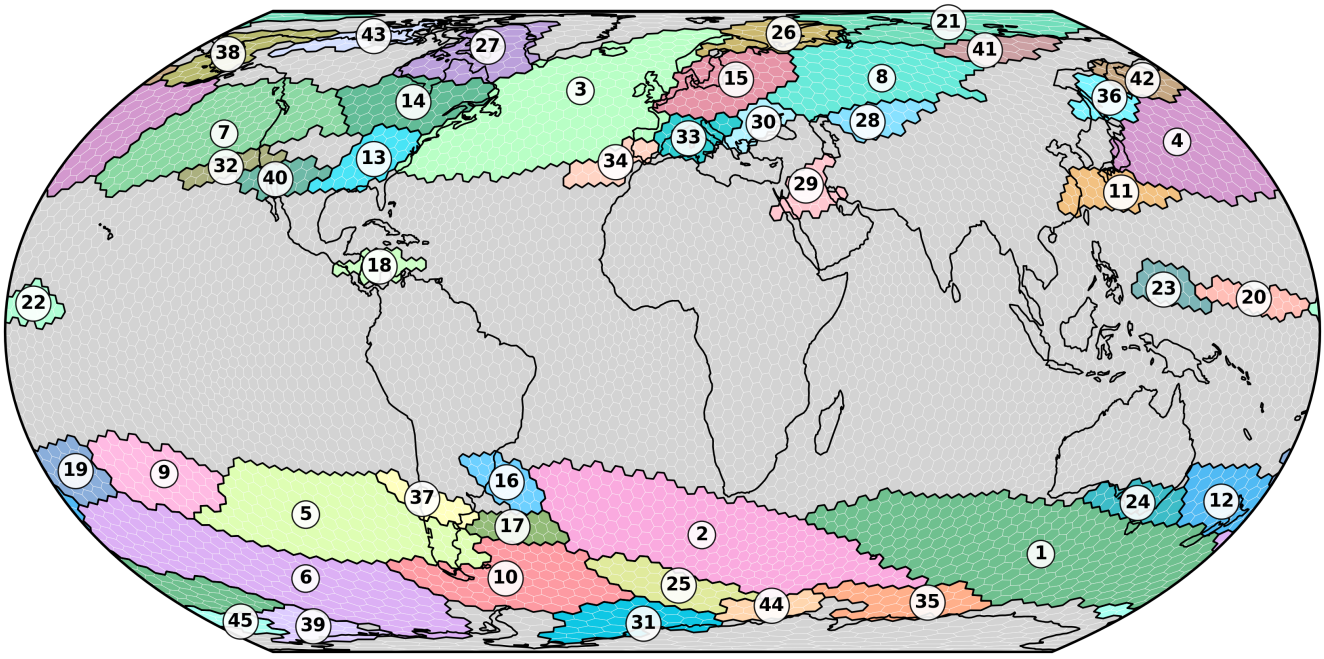

Figure S27. AR basins labeled consistently with table Tab. S1. The displayed partition is the most central partition, same as in Fig. 5 in the main manuscript. Basin labels are ascending in the order of how much time PIKART ARs have spent in the respective basin over the study period.

Table S1: Lifecycle characteristics of the AR basins identified by partitioning of the consensus network (PIKART + tARget-4) and analysis of PIKART AR trajectories. Values are averaged over all AR-timesteps assigned to each basin. **IVT**: integrated vapour transport (kg m^{-1} s^{-1}); **Area**: AR shape area (10^3 km^2); **Length**: AR axis length (km); **Land**: fraction of AR footprint over land (%); **Inland pen.**: frequency of inland-penetrating ARs (%); **Residence**: mean residence time per AR within the basin (hours). The bottom row gives the across-basin mean. Basin labels are ascending in the order of how much time PIKART ARs have spent in the respective basin over the study period.

Basin	IVT (kg m^{-1} s^{-1})	Area (10^3 km^2)	Length (km)	Land (%)	Inland pen. (%)	Residence (h)
1	492	1542	3722	2.1	2.9	53.7
2	533	1810	4007	0.9	1.6	59.4
3	553	1624	3727	7.5	20.8	60.6
4	603	2230	4331	1.9	13.5	59.5
5	537	1778	4053	2.4	13.7	52.8
6	454	1486	3615	0.7	3.6	34.9
7	546	1540	3653	7.3	24.3	40.2
8	289	1025	2849	97.5	13.6	30.7
9	570	1885	3716	0.0	9.2	37.6
10	395	1230	3138	2.8	4.8	23.1
11	584	2055	3741	20.3	8.3	26.6
12	488	1343	3163	5.8	2.5	26.4
13	503	1281	2769	84.8	5.1	24.2
14	427	1175	2876	85.0	5.8	24.1
15	354	1060	2770	80.6	34.1	21.5
16	550	1844	3879	32.1	1.2	21.1
17	503	1509	3378	8.2	5.5	18.1
18	506	1408	3177	9.5	16.5	39.1
19	545	1719	3439	0.2	6.4	23.1
20	510	2455	3990	0.1	1.4	29.8
21	192	874	2612	32.0	13.2	19.9
22	496	2996	4277	0.0	0.8	26.2
23	528	2451	3852	1.5	3.5	28.2
24	440	1376	3159	43.0	9.2	16.9
25	355	1247	3209	0.2	2.8	16.2
26	265	1029	2751	40.9	35.3	17.5
27	276	914	2639	44.3	14.4	18.0
28	279	981	2709	99.9	6.2	18.3
29	294	1136	2760	88.6	4.7	21.5
30	321	1096	2834	69.5	27.4	16.6
31	180	847	2532	3.4	6.6	14.7
32	485	1340	3089	9.5	35.7	16.1
33	375	961	2730	48.5	41.5	14.5
34	468	1282	3222	14.2	44.8	15.9
35	263	848	2581	3.6	3.9	12.7
36	409	1075	2862	26.4	6.9	16.0
37	398	1075	2892	36.4	25.3	10.6
38	284	933	2738	28.7	35.9	13.2

continued on next page

Table S1 (continued)

Basin	IVT (kg m^{-1} s^{-1})	Area (10^3 km^2)	Length (km)	Land (%)	Inland pen. (%)	Residence (h)
39	243	863	2600	4.0	11.4	13.1
40	299	995	2461	62.5	49.7	14.3
41	193	900	2596	90.0	6.3	13.7
42	353	978	2839	16.8	18.0	12.7
43	179	845	2435	61.0	24.3	12.3
44	209	823	2616	3.7	2.5	12.0
45	268	826	2483	0.6	3.6	11.0
mean	**400**	**1349**	**3144**	**28.4**	**14.0**	**24.6**

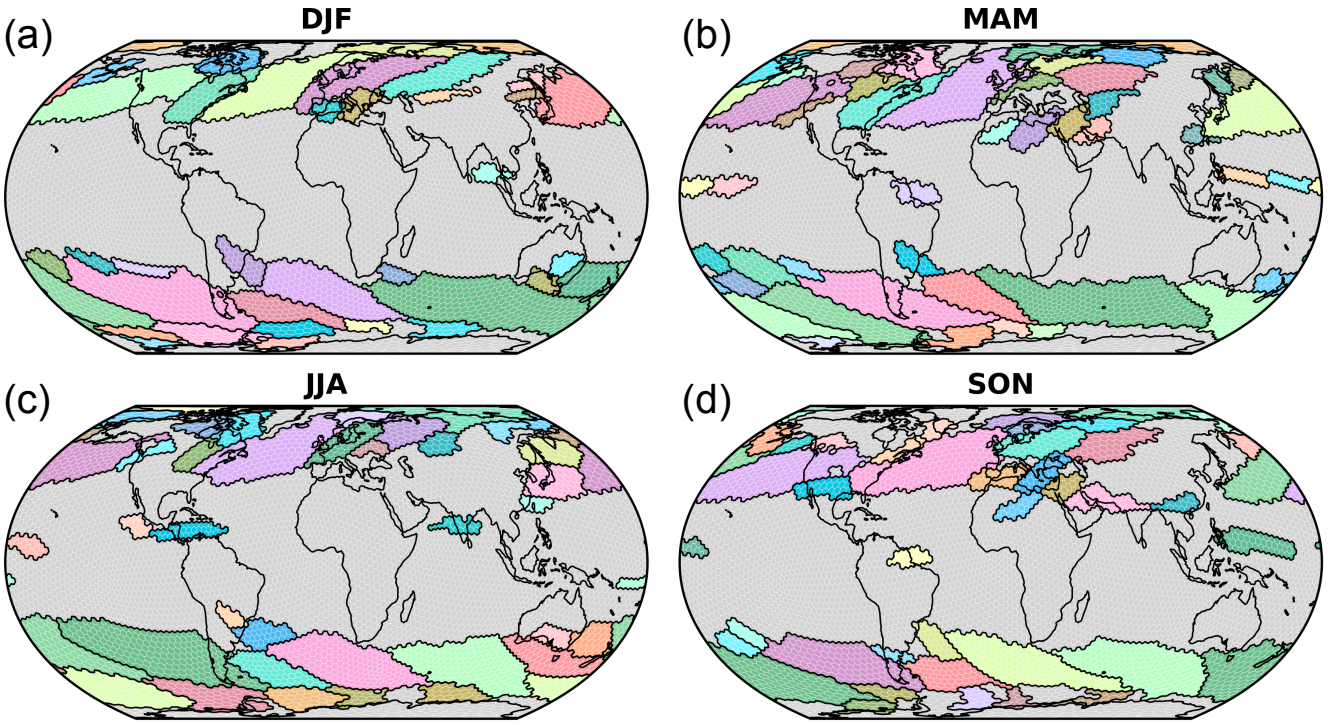

Figure S28. Seasonal AR basins. Same as Fig. 5 in the main manuscript, but from seasonal ARTNs.

References

Lora, J. M., Shields, C., and Rutz, J.: Consensus and disagreement in atmospheric river detection: ARTMIP global catalogues, Geophysical Research Letters, 47, e2020GL089 302, https://doi.org/10.1029/2020GL089302, 2020.

Maclennan, M. L., Winters, A. C., Shields, C. A., Thaker, R., Barthelemy, L., Codron, F., and Wille, J. D.: Rising atmospheric moisture escalates the future impact of atmospheric rivers in the Antarctic climate system, Communications Earth & Environment, 6, 1–10, https://doi.org/10.1038/s43247-025-02333-x, 2025.

Wang, Z., Ding, Q., Wu, R., Ballinger, T. J., Guan, B., Bozkurt, D., Nash, D., Baxter, I., Topál, D., Li, Z., Huang, G., Chen, W., Chen, S., Cao, X., and Chen, Z.: Role of atmospheric rivers in shaping long term Arctic moisture variability, Nature Communications, 15, 5505, https://doi.org/10.1038/s41467-024-49857-y, 2024.